American Mineralogist, Volume 78, pages 158–177, 1993

Disequilibrium decomposition and breakdown of muscovite in high *P-T* gneisses, Betic alpine belt (southern Spain)

ANTONIO GARCÍA-CASCO, ANTONIO SÁNCHEZ-NAVAS, RAFAEL LUIS TORRES-ROLDÁN
Departamento de Mineralogía y Petrología and I.A.G.M., Consejo Superior de Investigaciones Científicas, Universidad de Granada, Fuentenueva s/n, 18002-Granada, Spain

ABSTRACT

Muscovite from anatectic leucogneisses of the Torrox gneiss complex (Betic alpine belt, southern Spain) has an unusually wide range in composition. Primary matrix crystals are Si-rich (up to 6.66 atoms pfu, normalized to 20 O atoms and 4 OH) and contain abundant structurally controlled biotite + quartz intergrowths that range in size from a few nanometers to tens of micrometers. Diffusion halos, depleted in Si, Fe, and Mg, developed in muscovite around these intergrowths. Also, a continuous compositional trend of decreasing Si, Fe, Mg, and Ti and increasing Al, Na, and K was formed by primary and recrystallized matrix muscovite grains, the latter forming the end product of this evolution, with Si contents as low as 6.14 atoms pfu. Inspection of TEM images of the finer biotite intergrowths reveals that (1) these intergrowths represent a variety of frozen stages of growth, with interfaces that changed from coherent and semicoherent to incoherent upon coarsening, and (2) that biotite-quartz nucleation was probably influenced by deformation defects in the host muscovite. A third textural variety of muscovite appears as large, homogeneous, pegmatitic grains with low Si contents (6.13 atoms pfu), which underwent partial low-*P* breakdown to fibrolite + andalusite + potassium feldspar + biotite. The primary and recrystallized muscovite crystals do not bear indications of breakdown.

The textures and compositional features associated with the decomposition of the phengitic components of primary muscovite, and with the breakdown of the pegmatitic variety, suggest that the overstepping of the respective reaction boundaries was rapid. This is consistent with independent estimates of the *P-T-t* trajectory of the Torrox gneiss complex, which was characterized by rapid and marked decompression of approximately 10 kbar at high *T* (from >10 to 2 kbar, and from 650 to 600 °C) and was followed by very rapid cooling (>200 °C/m.y.) at low *P*. Phengitic decomposition took place during decompression and deformation, resulting in a wide range of intermediate compositions, the intergrown biotite + quartz assemblage, and the diffusion halos. The reaction textures and the residual composition of primary muscovite are interpreted in terms of a change in the rate-limiting step from surface- to diffusion-controlled growth upon coarsening of product phases. The absence of potassium feldspar in the product phase assemblage, which conflicts with the stable equilibrium relationships and mass balance calculations, indicates that K diffused to the matrix. Although decomposition proceeded probably far from equilibrium (i.e., strongly overstepped), it is suggested that it followed the theoretical behavior expected for muscovite solid solution, indicating that *P* substantially influences the Si content of high-grade muscovites similarly to what is well known in lower *T* environments. The metastable persistence of muscovite outside the subsolidus stability of muscovite + quartz is explained by a combination of (1) a *P-T* path that evolved near the muscovite-out isograd, (2) high rates of cooling and decompression at low *P*, and (3) moderate displacements in the *P-T* location of the equilibrium reaction due to compositional differences of the phases involved, most probably the fluid phase.

INTRODUCTION

Because of their widespread occurrence in many metamorphic and igneous rocks, muscovite solid solutions are important in the description and interpretation of natural systems. The major deviations of muscovite from its ideal composition, $K_2Al_4Al_2Si_6O_{20}(OH)_4$, are normally ascribed to two main solid solutions, the paragonite-muscovite series, involving the NaK_{-1} exchange component, and the phengite series, involving the Tschermak (tk, $SiMgAl_{-2}$) exchange component, which relates muscovite to the leucophyllite component $K_2Mg_2Al_2Si_8O_{20}(OH)_4$. These substitutions are known to be strongly influenced by intensive and extensive parameters and to display an

0003–004X/93/0102–0158$02.00

antipathetic behavior in muscovite solid solutions (see Guidotti, 1984, for a review). Natural phengitic muscovite also includes Fe^{2+} and Fe^{3+}, involving the $FeMg_{-1}$ and the $Fe^{3+}Al_{-1}$ exchanges (Wise and Eugster, 1964), the latter less well constrained and documented.

The deviation of muscovite from ideal composition as a result of the Tschermak substitution has been studied in natural, experimental, and theoretical model systems. For a given system, composition, and phase assemblage, a consistent decrease in the Si content of natural muscovite occurs with decreasing P and increasing T (e.g., Ernst, 1963; Cipriani et al., 1971; Guidotti and Sassi, 1976; Guidotti, 1984). The system composition and phase assemblage also exert an important control on the extent of substitution: at constant P-T conditions, muscovite from strongly aluminous compositions, bearing one or more Al-saturating phases, is more Al-rich and Si-poor than muscovite from less aluminous compositions that coexist with potassium feldspar (Guidotti, 1973; Miyashiro and Shido, 1985). The change in muscovite composition due to the Tschermak exchange within the limiting equilibrium assemblage Bt + Qtz + Kfs + H_2O (mineral abbreviations after Kretz, 1983) has been investigated by Velde (1965, 1967), Monier and Robert (1986a), and Massonne and Schreyer (1987). The model net-transfer reaction (J.B. Thompson, 1982b) describing the divariant equilibrium (KMASH system) is

$$\underset{\text{muscovite}}{3K_2Al_6Si_6O_{20}(OH)_4} + \underset{\text{Tschermak's substitution}}{6SiMgAl_{-2}} = \underset{\text{potassium feldspar}}{4KAlSi_3O_8} + \underset{\text{quartz}}{6SiO_2} + \underset{\text{biotite}}{K_2Mg_6Al_2Si_6O_{20}(OH)_4} + 4H_2O \quad (1)$$

written in terms of the Tschermak exchange vector to emphasize the increasing Al contents of the micas on decomposition (J.B. Thompson, 1979; A.B. Thompson, 1982). Si isopleths for Reaction 1 (further referred to as phengitic muscovite decomposition) have low positive dP/dT slopes (Velde, 1965, 1967; Massonne and Schreyer, 1987), indicating a strong pressure effect on the substitution, which is in good agreement with natural metamorphic muscovite.

The presence of reaction textures resulting from Reaction 1 helps constrain P-T paths (Massonne and Schreyer, 1987). Given the geometry of Si isopleths, reaction textures and associated compositional heterogeneities in muscovite are often found in high-P blueschist and eclogite facies metamorphic rocks that were subjected to decompression (e.g., Heinrich, 1982; Saliot and Velde, 1982; Franz et al., 1986; Evans and Patrick, 1987). Indications of instability of high-T phengitic muscovite are not so common; however, Ferrow et al. (1990) have presented evidence for exsolution of a 10-Å phyllosilicate, perhaps celadonite, within granitic muscovite. The lack of reaction textures caused by Reaction 1 in high-T muscovite is the result of (1) its low Si content, in most cases ranging from 6.1 to 6.3 atoms pfu (either metamorphic, e.g., Evans and Guidotti, 1966; Guidotti, 1973, 1978a; Tracy, 1978; Fletcher and Greenwood, 1979; Holdaway et al., 1988; or igneous, e.g., Guidotti, 1978b; Miller et al., 1981; Lee et al., 1981; Kistler et al., 1981; Price, 1983; Monier and Robert, 1986b; Sevigny et al., 1989), (2) the positive dP/dT slopes of reaction isopleths, in combination with P-T paths dominated by cooling, or (3) favorable kinetics under slow changes in P-T conditions and availability of fluids. However, that heterogeneous muscovite populations often develop within single samples, and even within individual crystals, in cooling plutonic bodies (e.g., Miller et al., 1981; Speer, 1984; Monier et al., 1984; Konings et al., 1988) indicates that muscovite equilibration is a sluggish process under high- to medium-temperature conditions.

The subsolidus upper stability of muscovite in SiO_2-saturated rocks is described by the univariant equilibrium (KASH system)

$$\underset{\text{muscovite}}{K_2Al_6Si_6O_{20}(OH)_4} + \underset{\text{quartz}}{2SiO_2} = \underset{\text{aluminum silicate}}{2Al_2SiO_5} + \underset{\text{potassium feldspar}}{2KAlSi_3O_8} + 2H_2O \quad (2a)$$

which is commonly considered as the low-T limit (isograd) for high-grade rocks. In spite of the discontinuous nature of Reaction 2a, muscovite can be found coexisting with Kfs + Qtz + aluminum silicate across a zone of persistence in high-T rocks subjected to prograde metamorphism at low to intermediate P. This zone might result from (1) kinetic factors (Kerrick et al., 1991), (2) the heterogeneous nature of fluids (e.g., Speer, 1982) as Reaction 2a is displaced to lower T at the condition $P_{H_2O} < P_{tot}$ (e.g., Kerrick, 1972), or (3) variations in the composition of the solid phases. Experimental and theoretical studies on Reaction 2a show that, under low to moderate overstepping of the reaction boundary, muscovite should rapidly react to completion (e.g., Ridley and Thompson, 1986; Schramke et al., 1987; Kerrick et al., 1991) and that the displacements of Reaction 2a in the P-T space due to variations in the composition of muscovite would not account for this zone of persistence. The reaction

$$\underset{\text{muscovite}}{K_2Al_6Si_6O_{20}(OH)_4} + \underset{\text{Tschermak's substitution}}{2x(SiMgAl_{-2})} + \underset{\text{quartz}}{(2-4x)SiO_2} = \underset{\text{aluminum silicate}}{(2-2x)Al_2SiO_5} + \underset{\text{potassium feldspar}}{(2-2x/3)KAlSi_3O_8} + \underset{\text{biotite}}{(x/3)K_2Mg_6Al_2Si_6O_{20}(OH)_4} + (2-2x/3)H_2O \quad (2b)$$

which includes the phengite components in muscovite and the production of a ferromagnesian phase (i.e., biotite, KMASH system), occurs at a point only a few degrees higher than Reaction 2a (A.B. Thompson, 1982), but this displacement is counterbalanced by the effect of

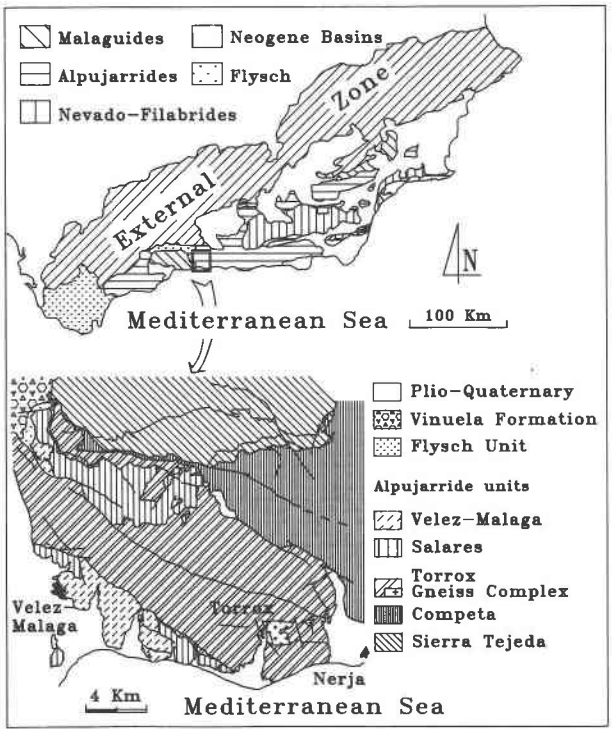

Fig. 1. Geologic sketch map of the Velez Malaga–Sierra Tejeda massif in the central Betic zone of the Betic Cordilleras. Location of TGC (Torrox gneiss complex) is shown. Lithologic sequences are not differentiated within units. Based on an unpublished map by R.L. Torres-Roldán (see Torres-Roldán, 1979; Elorza and García-Dueñas, 1981; Sanz de Galdeano, 1989, for an explanation of these regional terms and further geologic information).

Na in the micas and feldspars (e.g., Chatterjee and Froese, 1975). Indications for Reaction 2 (either 2a or 2b, further referred to as muscovite breakdown) are not common in high-*P*, medium-to-high *T* rocks subjected to decompression, indicating that the *P-T* paths followed by high-*P* rocks are normally dominated by cooling at intermediate to low pressure.

In this paper we document what appears to be a rare natural case of phengitic muscovite decomposition (product assemblage Bt + Qtz) and breakdown (product assemblage And or fibrous sillimanite + Kfs + Bt) in high *P-T* anatectic leucogneisses (Torrox gneiss complex, southern Spain). Complex reaction microtextures and wide compositional heterogeneities developed within these muscovites as the result of a tectonic setting that caused the original high *P-T* assemblages to undergo rapid near-isothermal decompression at high temperature.

Field and petrological setting

The Torrox gneiss complex (TGC) is a heterogeneous gneissic body that is located in the central segment of the Betic Cordilleras, about 50 km east of Málaga; the area includes several Alpujarride, Malaguide, and flysch tectonic units (Fig. 1). The TGC crops out (~3 km^2 and >500 m thick) at the bottom of the upper Alpujarride unit in the area (Torrox unit; Fig. 1), beneath a thick sequence of amphibolite facies graphitic schists. Both the graphitic schists and the TGC gneisses experienced a similar deformational and metamorphic history during the Alpine orogeny. The latest penetrative synmetamorphic deformation event resulted in the dominant megascopic mylonitic foliation (D_2, of Cuevas et al., 1989). Assemblages in the system A-F-M-Ti in the graphitic metapelites adjacent to the gneissic body include pre-S_2 Ms + St + Grt + Bt + Ky + Rt, syn-S_2 fibrous sillimanite + St + Bt + Ilm, and post-S_2 And + Bt + Ilm ± Crd. All three aluminum silicate polymorphs coexist in most samples, and a complex mineral growth and dissolution history can be deduced from the textures and compositions of the minerals. Fibrous sillimanite + Bt + Ilm and And + Bt + Ilm pseudomorphs after staurolite, Bt + Ms ± Pl after garnet, Crd + Bt after garnet and staurolite, and replacement of kyanite by andalusite indicate that lower *P* assemblages evolved from higher *P* assemblages by means of staurolite and garnet breakdown reactions upon decompression. Comparable examples of frozen disequilibrium are common in other Alpujarride sequences (Loomis, 1976, 1979; Torres-Roldán, 1974, 1981). Uniform cooling ages for numerous minerals in several isotopic systems (cooling ages cluster around 21 ± 2 Ma; Zeck et al., 1989, 1992; Monié et al., 1991a, 1991b) suggest that rapid cooling followed rapid decompression, precluding complete reequilibration at low pressure.

Within the TGC the main type of rock is a medium-grained granitic leucogneiss. In addition to quartz, sodic plagioclase, and potassium feldspar, the other major phases are muscovite and biotite (up to 10–20%) and, in some cases, garnet (<5%). Accessory minerals include abundant apatite and tourmaline, whereas zircon, ilmenite, rutile, kyanite, sillimanite, andalusite, and dumortierite are less commonplace. Three main varieties of leucocratic gneiss can be differentiated in terms of their textural, phase-assemblage, and outcrop characteristics: muscovite biotite garnet banded gneiss, augen and porphyritic muscovite biotite gneiss, and muscovite garnet biotite aplites containing muscovite, tourmaline, and spessartine garnet with pegmatitic sizes. The porphyritic muscovite biotite gneiss contains centimeter-sized aluminous enclaves (restites) with a primary assemblage of Bt + Ky + Rt + Grt + Ap + graphite, which is overprinted by sillimanite, andalusite, ilmenite, and muscovite. Nongranitic rocks also appear interbedded with the gneisses, including graphitic pelitic layers with variable amounts of muscovite, quartz, biotite, garnet, aluminium silicates, feldspars, ilmenite, rutile, graphite, apatite, zircon, and tourmaline. All these rock types occur as strongly foliated layers or lensoid bodies, with the exception of some porphyritic muscovite biotite gneisses and the aplites. The latter form concordant layers and centimeter- to meter-sized pods and dikes with relationships that are diffuse to sharply crosscutting, suggesting an origin by

short-range melt segregation. Due to strong deformation and alpine metamorphism (which includes small to moderate amounts of partial melting), as well as its lithologic heterogeneity, the origin of the TGC as a whole is still uncertain. Alternative hypotheses range from a metasedimentary derivation to a prealpine anatectic gneiss.

Sample description

The muscovite populations from four banded muscovite biotite garnet gneiss samples were studied. Phase assemblages in the four samples are fairly homogeneous. In addition to the main granitic matrix assemblage Qtz + Pl + Kfs, these samples consist of Ms + Bt + Grt and abundant, coarse, rounded, apatite crystals (up to 0.5 mm in size). Potassium feldspar also forms megacrysts that include idiomorphic plagioclase crystals with inverse zoning and xenomorphic cores. These megacrysts show intense deformation and sigmoid tails. Matrix biotite is not abundant (ca. 5%), and occurs parallel to the main foliation defined by muscovite. Medium- to fine-grained garnet is always present (<5%), has corroded rims, and is partly replaced by medium- to fine-grained aggregates of Ms + Bt ± Pl ± Qtz and by late retrograde (green) biotite. Accessory phases include tourmaline and very scarce fine-grained rutile and ilmenite. No aluminum silicate polymorphs were detected in the matrix of the analyzed samples.

In all samples muscovite is more abundant than biotite. With the exception of scarce retrograde aggregates after potassium feldspar, three main textural types of muscovite habits can be distinguished: primary deformed matrix crystals, recrystallized matrix grains, and large pegmatitic crystals. Primary muscovite crystals have textural characteristics that suggest equilibrium with the enclosing granitic gneiss. In the samples investigated, deformation textures and microfabrics are commonplace, but muscovite still has a medium- to coarse-grained booklet habit (0.5–2 mm), and it has clean, sharp contacts with feldspars. Associated with primary crystals are biotite-quartz (+ minor occasional rutile) intergrowths on the optical to TEM scale (10–30 μm to 10^{-3} μm, see below), oriented parallel to (001) planes of the host muscovite. Recrystallized muscovite grains have resulted from shear deformation and grain-size reduction of primary crystals. They appear as randomly oriented fine-grained grains (<0.5 mm) associated with primary deformed crystals. Some of these recrystallized grains also contain thin intergrowths of biotite, similar to but much less abundant than those within primary grains. Pegmatitic crystals, up to 5 cm long and 1.5 cm across, appear less commonly within the muscovite biotite garnet banded gneisses, and particularly in one of the samples selected for detailed study (T506). These larger muscovite crystals are typically associated with coarse tourmaline and form the core of sparse augen-like structures, with a microgranular outer rim of quartz, potassium feldspar, and albite. The augen structures, which are deformed and lie parallel to the foliation of the rock, are interpreted as pegmatitic segregations that formed close to the H_2O-saturated granitic solidus. These pegmatitic muscovite samples bear partial pseudomorphs consisting of coarse-grained And or fibrous sillimanite + Kfs + Bt, which are not observed in the primary and recrystallized matrix muscovite.

Analytical procedures

An automated Cameca SX50 electron microprobe (University of Granada), operated at 20 kV, was used to determine mineral compositions. Data were reduced using a ϕ-ρ-z procedure supplied by the manufacturer (see Pouchou and Pichoir, 1985, for details), using simple oxides (Al_2O_3, Fe_2O_3, $MnTiO_4$, MgO) and silicates (albite, orthoclase, wollastonite) as calibration standards. Detailed wavelength scans indicated no appreciable amounts of other elements such as Ba, Sr, and Cl in the micas. F might be present in low amounts, but could not be reliably estimated on a routine basis. In the case of muscovite, special care was taken to locate the electron beam on areas where no intergrown phases appeared at the scale of optical and backscattered electron (BSE) images. For muscovite, biotite, and feldspars, operating parameters were optimized to avoid alkali loss, after the results of a number of experiments, as illustrated in Figure 2. In accordance with the results of these experiments, both Na and K were always counted first (simultaneously) and beam current and probe sizes were combined so as to use current densities of ca. 0.8 nA μm^{-2}, for which no appreciable decrease in counting statistics was expected during their counting times (15–25 s). However, large current densities (up to 20 nA μm^{-2}) had to be used for small biotite intergrowths (5 nA, 0.25-μm^2 probe size). Representative mica compositions are listed in Table 1 (see Appendix Tables 1 and 2[1] for the complete set of 66 spot analyses of muscovite studied and representative compositions of coexisting phases, respectively).

The TEM images were obtained with a Zeiss EM10C (University of Granada), operated at 100 keV. An objective aperture of 40 μm, corresponding to a minimum d_{hkl} value of 0.35 nm, was selected to allow adding 001 diffracted and 000 transmitted beams to achieve a compromise between amplitude contrast and phase contrast in the images. TEM specimens, selected from specially prepared thin sections, were thinned using Ar ion-beam techniques to obtain electron-transparent edges. Qualitative analyses were performed with a Jeol 1200-EX equipped with a LINK energy-dispersive X-ray spectrometer (University of Cádiz) operated at 120 keV and with a spot size of 100 nm to help with the identification of TEM-scale intergrowths within primary muscovite.

[1] A copy of Appendix Tables 1 and 2 may be ordered as Document AM-93-514 from the Business Office, Mineralogical Society of America, 1130 Seventeenth Street NW, Suite 330, Washington, DC 20036, U.S.A. Please remit $5.00 in advance for the microfiche.

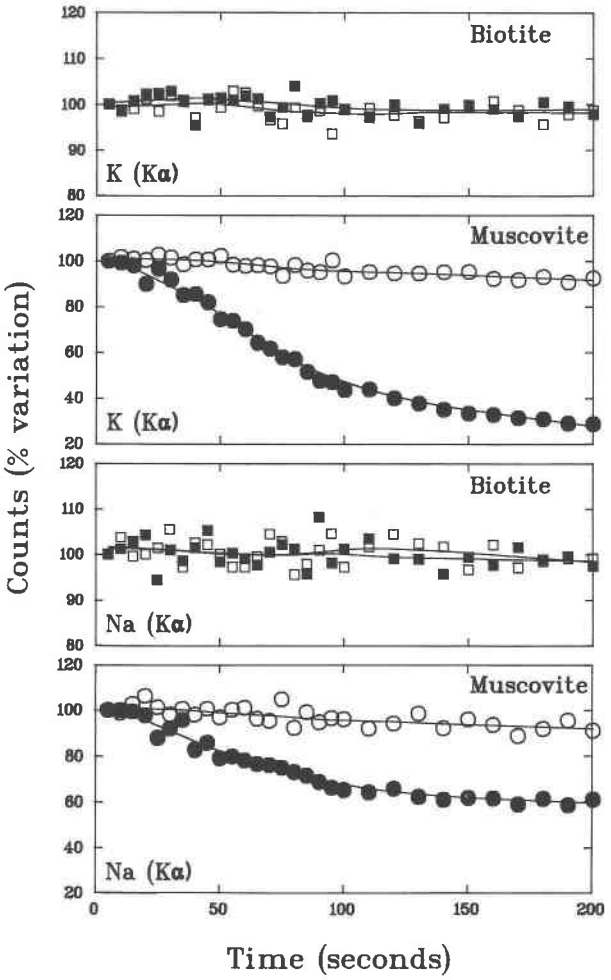

Fig. 2. Plots showing the effect of the duration of electron bombardment on measured X-ray intensities of Na and K in micas. The diagrams represent the percent variation in counting rates (counts/second) during successive 10- and 20-s intervals relative to the initial 10-s integration period. The data were obtained during single continuous analyses on the same spot of micas from sample T313 referred to in the text, using a constant acceleration potential of 20 kV. The results of experiments using probe current densities of 0.8 nA/μm^2 (open symbols) and 20 nA/μm^2 (solid symbols) are shown for comparison. The plots indicate that no significant alkali mobilization takes place during the initial 50 s when moderate current densities of about 1 nA/μm^2 are used (e.g., 20 nA with a probe diameter of about 5–6 μm). For biotite, the same applies up to much higher probe current densities, which allowed the use of a probe size of approximately 0.25 μm^2 to analyze small biotite intergrowths within muscovite.

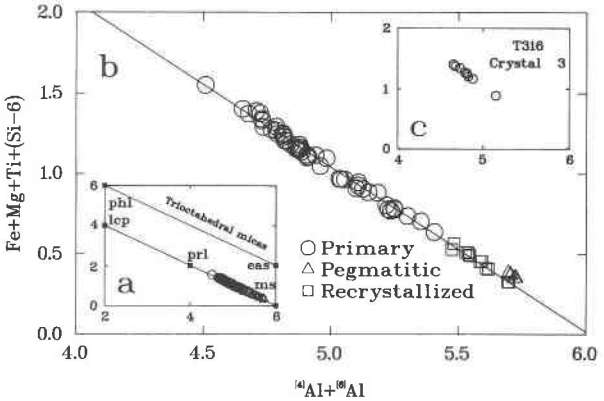

Fig. 3. (**a**) Multicationic diagram including relevant mica end-members to illustrate the continuous nature of the coupled cation substitutions underlying the compositional variations within the investigated muscovite populations. Abbreviations are explained in the text and Figure 12, except eas, which stands for the eastonite end-member [$K_2{}^{[6]}Al_2Mg_4Al_4Si_4O_{20}(OH)_4$]. (**b**) Enlarged section of the plot in (**a**), including a regression on the primary and recrystallized grains. Note the progressive increase in the trioctahedral contents as compositions deviate from the muscovite end-member. Higher apparent trioctahedral contents of the pegmatitic type are inferred to be caused by high Fe^{3+}/Fe^{2+} ratios. (**c**) Compositional variation within a representative single primary crystal from sample T316.

Mineral composition

Muscovite

A continuous compositional spectrum is formed by the primary and recrystallized grains (Figs. 3, 4). The group of primary muscovite samples exhibits the widest inter- and intragrain compositional range. Recrystallized grains show a much narrower intergrain compositional range, and individual crystals are homogeneous within analytical uncertainty. Because of the heterogeneous nature of individual primary crystals, we have used the complete set of analyses reported in Appendix Table 1, which represents single spot compositions located within compositionally homogeneous portions at the scale of BSE images. Compositional changes in the matrix grains (primary and recrystallized) include a decrease in Si (6.66–6.14 atoms pfu), Fe (0.46–0.10), Mg (0.33–0.05), Ti (0.13–0.01), and an increase in $^{[4]}Al$ (1.34–1.86), $^{[6]}Al$ (3.17–3.84), Na (0.10–0.20), K (1.62–1.77), and total interlayer occupancy (1.74–1.94). The octahedral occupancy compares well with other published analyses of muscovite (cf. Miller et al., 1981; Guidotti, 1984) and decreases (4.10–4.00) as primary muscovite becomes depleted in Fe and Mg (Fig. 4). The good correlations found among Si, Mg, Fe, Fe + Mg, and $^{[6]}Al$ (Fig. 4, Table 2) indicate that the progress of Reaction 1 is responsible for the largest fraction of the observed compositional variations in matrix muscovite. On the other hand, the pegmatitic muscovite grains form a homogeneous compositional group (Figs. 3, 4). Their composition overlaps with recrystallized grains having the lowest Si values (mean 6.13 atoms pfu, Table 1); however, pegmatitic muscovite has a lower alkali content (Fig. 4).

The presence of Fe^{3+} in matrix muscovite is implied by the relatively poor correlations of Fe with Si and $^{[6]}Al$, as compared with those of Mg, and the positive correlation between Fe and total octahedral cations (Fig. 4, Table 2). Normalizing to 44 negative charges with Fe^{3+} unaccounted for results in an overestimation of all cations in the structural formula, thus increasing the calculated

TABLE 1. Representative analyses of muscovite (single spots) and biotite

	Muscovite			Biotite			
				T336			
				Matrix		Intergrown*	
	T316 Prm* Spot 1	T336 Rcrt* Spot 79	T506 Pegm Spot 12	Mean (n = 11)	σ	Mean (n = 2)	σ
SiO_2	48.96	45.76	46.53	34.432	0.649	34.695	0.146
TiO_2	1.27	0.21	0.10	2.867	0.208	3.338	0.067
Al_2O_3	28.11	36.03	36.87	19.339	0.462	19.452	0.148
Cr_2O_3	0.00	0.03	0.00	0.014	0.016	nd	
FeO	3.67	1.01	1.49	24.267	0.775	22.614	0.036
MnO	0.06	0.02	0.02	0.148	0.027	0.165	0.004
MgO	1.65	0.26	0.26	4.407	0.203	4.800	0.093
CaO	0.01	0.01	0.00	0.016	0.017	0.010	0.010
Na_2O	0.42	0.77	0.68	0.195	0.046	0.138	0.033
K_2O	9.68	10.17	10.13	8.875	0.071	8.691	0.036
Total	93.82	94.27	96.06	94.561	0.335	93.900	0.132
H_2O**	4.407	4.472	4.556	3.823	0.019	3.835	0.007
Si	6.661	6.136	6.124	5.401	0.083	5.425	0.013
$^{[4]}$Al	1.339	1.864	1.876	2.599	0.083	2.575	0.013
$^{[6]}$Al	3.169	3.830	3.843	0.977	0.039	1.010	0.021
Cr	0.000	0.003	0.000	0.002	0.002	nd	
Ti	0.130	0.021	0.010	0.338	0.024	0.392	0.007
Fe	0.417	0.113	0.164	3.184	0.113	2.957	0.001
Mn	0.007	0.003	0.002	0.020	0.004	0.022	0.001
Mg	0.334	0.052	0.051	1.030	0.043	1.119	0.020
$^{[6]}\Sigma$	4.057	4.023	4.069	5.551	0.057	5.501	0.005
Ca	0.001	0.001	0.000	0.003	0.003	0.002	0.002
Na	0.112	0.200	0.174	0.059	0.014	0.042	0.010
K	1.681	1.740	1.700	1.776	0.019	1.734	0.010
$^{[12]}\Sigma$	1.794	1.942	1.874	1.838	0.013	1.777	0.019

Note: Total Fe expressed as FeO. Cations normalized to 20 O atoms and 4 OH; n = number of analyses; nd = not determined. Petrographic groups of muscovite: Prm = primary, Rcrt = recrystallized, and Pegm = pegmatitic grains (see Appendix Table 1 for the complete set of analyses). Matrix biotite represents an average of high-Ti (>0.3 atoms pfu) compositions (see text), and the intergrown biotite corresponds to the biggest lamellae occurring within the primary muscovite crystal of Figure 5.

* Analyses used in the mass balance calculations (Eq. 7 in the text).

** Calculated H_2O wt% on the basis of 4 OH pfu.

octahedral occupancies. The recrystallized and pegmatitic grains have a higher octahedral occupancy (mean of 4.03 and 4.07, respectively) than expected as a continuation of the trend formed by the primary grains and relative to their Fe + Mg contents (Figs. 3, 4). This suggests that the Fe^{3+}/Fe^{2+} ratio in these muscovite grains is higher. The presence of Fe^{3+} might also account for the ratio Fe/Mg > 1 in our samples, which increase from the primary (mean 1.178, σ = 0.236) to the recrystallized (mean 1.808, σ = 0.282) and pegmatitic (mean 3.214, σ = 0.505) grains, as compared with the experimentally determined greater relative solubility of Mg in muscovite (Velde, 1965, 1967; Monier and Robert, 1986a). Any rigorous evaluation of the Fe^{3+} contents in the muscovite is precluded by the probable occurrence of octahedral occupancy in excess of 4 atoms pfu (Monier and Robert, 1986a; Massonne and Schreyer, 1987), as the amount of the calculated Fe^{3+} (normalizing to eight tetrahedral plus four octahedral cations and 44 negative charges) is proportional to the octahedral occupancy (normalizing to 22 O). However, the formulae that include calculated Fe^{3+} can be considered as end-member estimates. For matrix muscovite, these calculations resulted in a slight modification of the compositional ranges of the major elements and little or no change of the minor elements (compare the ranges given above with Si = 6.63–6.12, $^{[6]}$Al = 3.82–

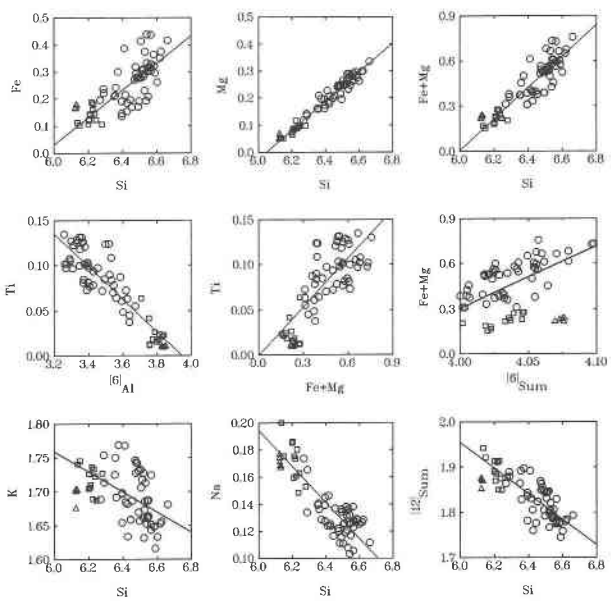

Fig. 4. Selected bivariate diagrams showing the compositional spectrum of the entire muscovite data set. Circles = primary grains. Squares = recrystallized grains. Triangles = pegmatitic grains. The regression lines do not include the pegmatitic grains.

TABLE 2. Pearson correlation matrix of selected variables for primary and recrystallized muscovite

	Si	$^{[6]}$Al	Ti	Fe	Mg	$^{[6]}\Sigma$	Na	K	$^{[12]}\Sigma$	Na/K	Fe + Mg
Si	1.000										
$^{[6]}$Al	−0.932	1.000									
Ti	0.813	−0.888	1.000								
Fe	0.765	−0.911	0.674	1.000							
Mg	0.975	−0.978	0.851	0.854	1.000						
$^{[6]}\Sigma$	0.225	−0.408	0.098	0.715	0.363	1.000					
Na	−0.838	0.853	−0.849	−0.671	−0.863	−0.149	1.000				
K	−0.538	0.321	−0.275	−0.196	−0.453	−0.156	0.214	1.000			
$^{[12]}\Sigma$	−0.814	0.649	−0.610	−0.465	−0.758	−0.192	0.630	0.893	1.000		
Na/K	−0.781	0.826	−0.827	−0.657	−0.818	−0.130	0.991	0.080	0.519	1.000	
Fe + Mg	0.893	−0.978	0.784	0.970	0.955	0.576	−0.786	−0.322	−0.619	−0.758	1.000

Note: Number of observations: 61.

3.12, Mg = 0.33–0.05, Ti = 0.13–0.01, Na = 0.20–0.10, and K = 1.76–1.61), indicating that only minor errors are introduced in the other components by the chosen normalization, with Fe_{tot} as Fe^{2+}. This is not the case with regard to the pegmatitic muscovite, whose octahedral occupancy is largely overestimated as a probable consequence of very high Fe^{3+}/Fe^{2+} ratios (see below).

Other minerals

Biotite also exhibits strong intergrain heterogeneities (Appendix Table 2). Matrix crystals are Ti-rich (>0.3 atoms pfu), intermediate Ti contents are found in biotite pseudomorphs (+ Ms + Pl) after garnet, and low-Ti (<0.1 atoms pfu) crystals are retrograde pseudomorphs after garnet. This indicates that garnet-consuming reactions are responsible for the change in composition of the matrix biotite crystals. The decrease in Ti involves a parallel increase in $^{[6]}$Al, Fe, and octahedral occupancy and a decrease in Mg. On the other hand, the composition of intergrown biotite within primary and pegmatitic muscovite is relatively Ti-rich (0.39 and 0.25 atoms pfu, respectively, Table 1 and Appendix Table 2). Garnet is normally unzoned, being rich in Fe and Ca ($x_{Grs} > 0.2$) and poor in Mg and Mn ($x_{Sps} < 0.03$, Appendix Table 2). Lower Ca and higher Mn contents are recorded in some fine-grained crystals and in thin rims (up to 50 μm) of the coarser grains. This zonation is crosscut by the Ms + Bt + Pl pseudomorphs. Plagioclase is rich in albite (Appendix Table 2). The compositional variations within individual samples are related to several stages of growth, involving a progressive increase in the anorthite content. In sample T313, crystals included in Kfs megacrysts appear with a slight reverse zoning with xenomorphic cores ($x_{An} = 0.09$) and idiomorphic overgrowths ($x_{An} = 0.13$), whereas matrix grains are homogeneous ($x_{An} = 0.14$). Within the pseudomorphs after garnet, plagioclase bears higher anorthite contents ($x_{An} = 0.19$). Potassium feldspar also has minor compositional intergrain heterogeneities within individual samples (Appendix Table 2), being slightly less albitic in the fine-grained matrix grains ($x_{Ab} = 0.19–0.18$), as opposed to the larger grains ($x_{Ab} = 0.23–0.21$), except when the latter appear slightly exsolved (e.g., T313, $x_{Ab} = 0.18$).

MICROTEXTURES

Primary and recrystallized muscovite

The compositional heterogeneities within individual primary muscovite grains are generally associated with the biotite-quartz intergrowths. Halos depleted in Si, Fe, and Mg and enriched in Al develop close to these intergrowths (Fig. 5), indicating that they were produced by phengitic decomposition of primary muscovite, in agreement with the observed bulk compositional changes of matrix muscovite (Fig. 4). The discontinuous and irregular outer rims appear to be related to the formation of larger biotite grains and overgrowths and to grain-size reduction and recrystallization at the edges of the crystals (Fig. 5A), although internally recrystallized grains are also apparent (Fig. 5A, 5B). Since recrystallized grains are the end product of the main compositional trend of primary crystals bearing Bt + Qtz intergrowths (Figs. 3, 4), their compositions can be directly related to the same continuous reaction affecting the primary muscovite. In the following paragraphs microtextural observations related to the mechanism of generation of the biotite-quartz intergrowths are summarized, shedding light on the kinetics of primary muscovite decomposition.

Heterogeneous nucleation. A variety of defects and defective areas appear over broad areas of primary muscovite grains. Most of these are deformational structures resulting from the shear deformation suffered by these rocks, and they include abundant stacking faults, elastic bending of the layers, edge dislocations (Fig. 6), and local pull-apart microstructures (Fig. 7). Because the stored elastic and surface energy reduces the activation energy required for the formation of a nucleus of critical size, defects are favorable nucleation sites (e.g., Putnis and McConnell, 1980; Lasaga, 1981; Ridley and Thompson, 1986). In our images, this is reflected by the abundance of small intergrowths (i.e., abundant nucleation sites). A particular case was found in relation with pull-apart microstructures. These microstructures formed as voids and microcracks along (001) planes (Fig. 7), probably along the interlayer region, which contains large and less strongly bonded cations (Veblen, 1983). In the example illustrated in Figure 7, the plastic strain is stored as two opposite

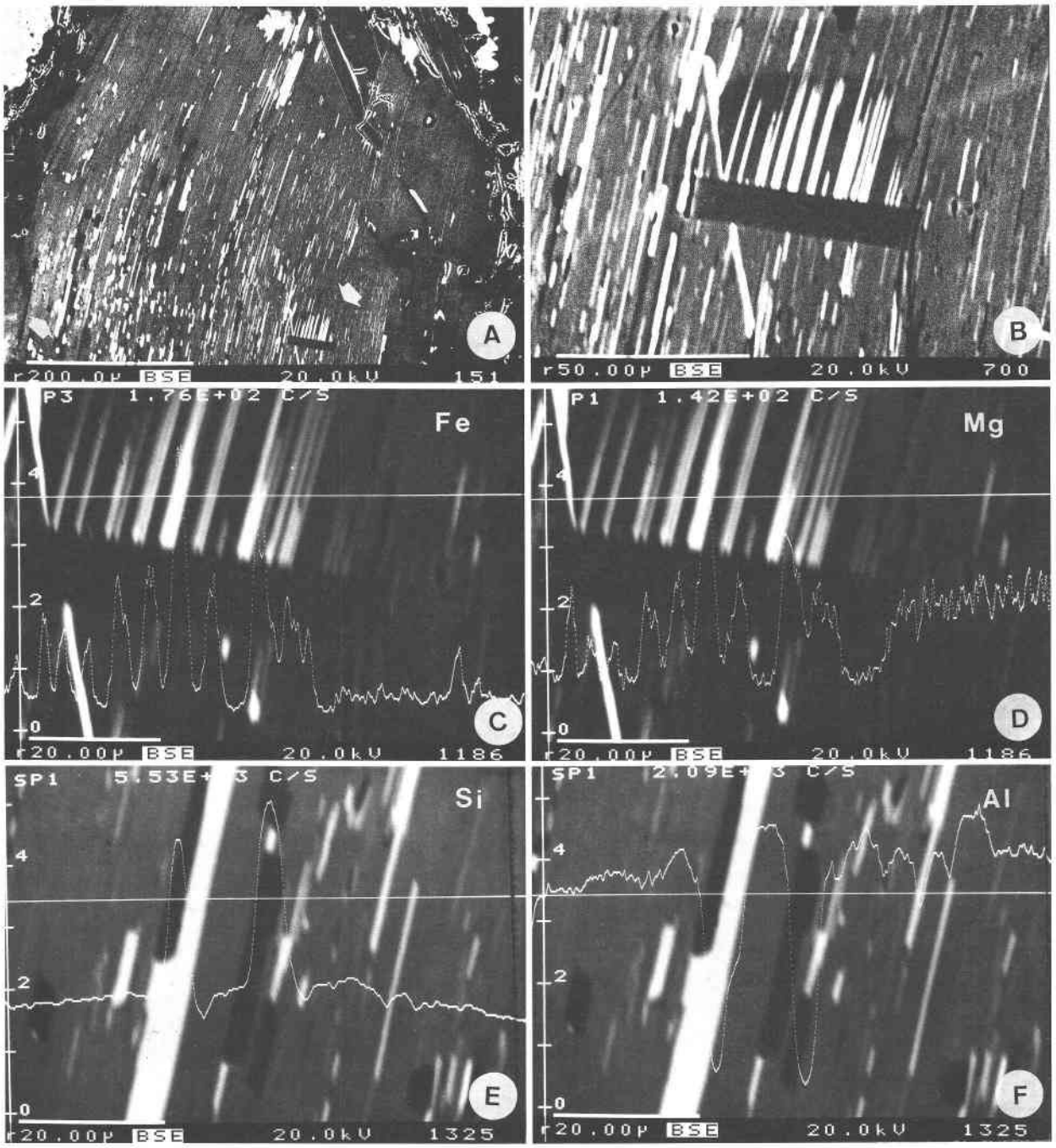

Fig. 5. BSE images and qualitative element traverses from a primary muscovite crystal from sample T336 bearing abundant Bt + Qtz intergrowths. (**A**) Low-magnification view of the crystal. The abundant biotite lamellae (bright white zones) and quartz inclusions (dark rods) parallel to the (001) planes of muscovite stand out clearly. Muscovite appears as various shades of gray. Note the irregular outer rim, and the patchy diffusion zoning within muscovite. Recrystallized muscovite grains appear as high-angle inclusions and at the edges of the primary muscovite. (**B**), (**C**), and (**D**) Enlarged area marked by arrow in **A** showing Fe and Mg depletion halos (dark gray) in muscovite (gray) close to intergrown biotite (white), and a tabular dark recrystallized muscovite grain. (**E**) and (**F**) Enlarged area marked by arrow in **A** showing elongated rods of quartz (black) and biotite laths (white) and the depletion in Si and enrichment in Al of muscovite (gray) close to the intergrowths. The qualitative element traverses are expressed in counts per second.

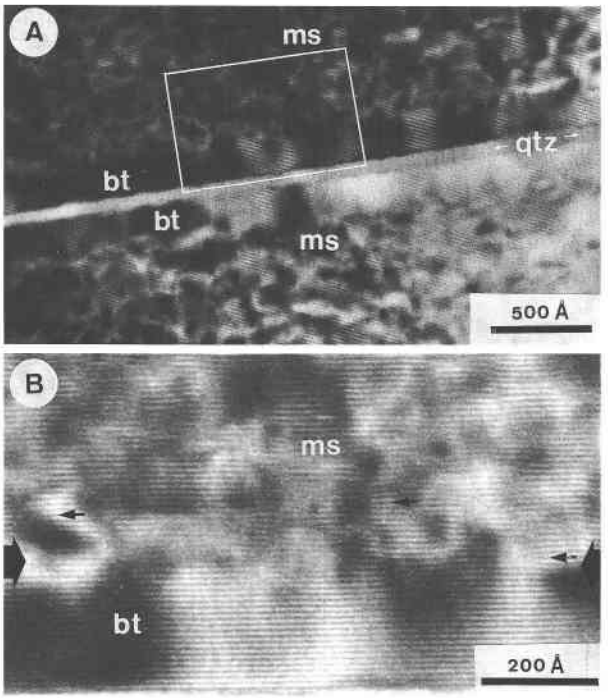

Fig. 6. TEM images of a composite intergrowth, within a primary muscovite host, consisting of two 200-Å biotite lamellae separated by an inner low-contrast (quartz?) band. (**A**) Low-magnification electron micrograph of this threefold microstructure. (**B**) An enlarged image of the region outlined in **A** showing abundant defective areas (thin arrows) consisting of elastic bending of the layers and edge dislocations in muscovite. Biotite lamellae show only minor deformation as compared with muscovite. The semicoherent muscovite-biotite interface is indicated by the thicker arrows: no change in orientation along **a** and **b** directions of the micas across the interface is inferred from the absence of marked contrast.

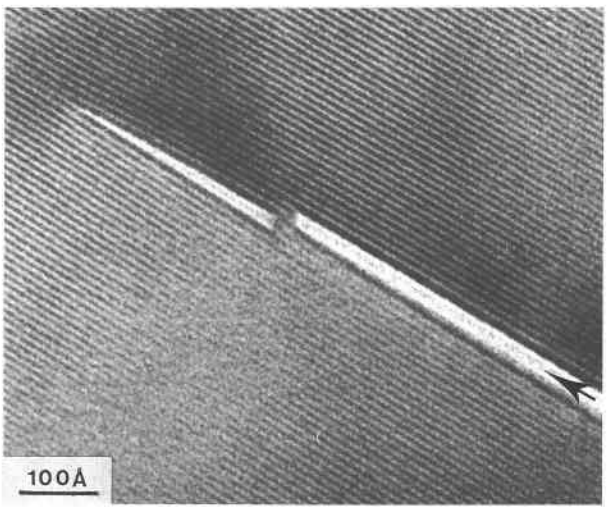

Fig. 7. Shear pull-apart microstructure parallel to the muscovite layers. Two edge dislocations within muscovite disrupt the structure that probably grew through a climb process. The two poorly defined extra fringes that appear attached to these coupled edge dislocations might represent single atomic rows of a growing phase (biotite?) in the void or Fresnel fringes at the edges of the mica along these gaps.

edge dislocations, so that the initial continuity between the two muscovite layers affected by the pulling apart is actually disrupted. In this figure, two poorly defined single fringes (the arrowed darker fringe inside the lighter area of low electron density) appear attached to the two edge dislocations disrupting muscovite. These extra fringes could be single atomic rows of a quenched ångström-sized phase (biotite?) growing in the void as the microstructure migrates through the climb of the edge dislocations. An alternative interpretation is that these apparent extra fringes do not actually result from an extra layer, but rather from the Fresnel fringes at the edges of the mica along these gaps (see also Eggleton and Buseck, 1980).

Semicoherent growth. TEM images further confirm the evidence for structurally controlled (interface-controlled) growth of biotite, and to a lesser extent quartz, parallel to (001) planes of the micas. However, variable degrees of apparent coherency relative to the **c*** direction (Figs. 6, 8, 9) were found to be related to the grain size of the biotite lamellae, and thus to different stages of growth. The coincidence of the **c*** axes of muscovite and very thin biotite lamellae is indicated by lattice fringes with 10-Å spacing in both phases (Fig. 8). Since Figure 8 is not a structure image, no direct information can be gained relative to the structural continuity along other directions. However, the lack of boundaries with sharp contrast, such as those related to stacking faults of micas or other phyllosilicates (e.g., Veblen, 1983, his Fig. 2), which would indicate a change in orientation in **a** and **b** directions of the lamellae (D. R. Veblen, personal communication, 1991), suggests the development of semicoherent (001) interfaces for this very thin lamella (i.e., during the initial stages of growth).

The above structural relations suggest that (001) planes might have acted as optimal phase boundaries (Robinson et al., 1971) for both micas, in spite of the fact that their different a and b dimensions would make an exact fit of both structures along (001) planes impossible (see Iijima and Zhu, 1982, for coherent biotite-muscovite intergrowths perpendicular to mica layers). The a and b dimensions are related to the coplanarity of the basal O of the tetrahedral layers and the geometry of the octahedral coordination in micas and are a function of the octahedral cations and occupancy (Zussman, 1979; Weiss et al., 1985). Thus, coherence was favored during initial stages of growth by the higher phengite contents of the host muscovite (i.e., by its greater a and b dimensions; Zussman, 1979; Massonne and Schreyer, 1986), although it was not maintained with further decomposition as the a and b dimensions of muscovite shrink. With continued decomposition and biotite growth, the elastic strain fields at the semicoherent interfaces would be expected to be-

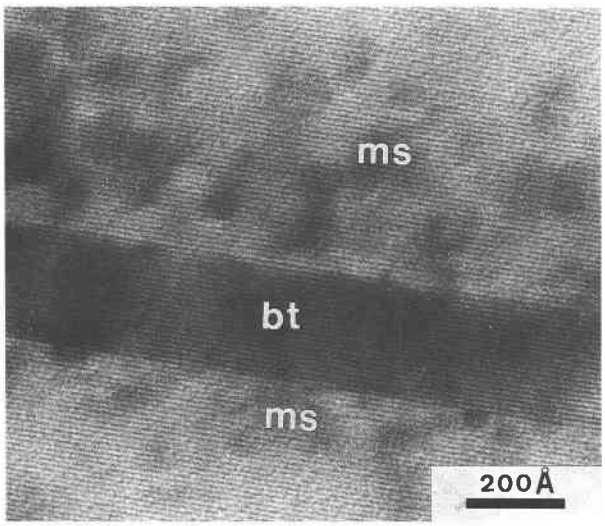

Fig. 8. Semicoherent biotite lamella (dark) within muscovite. Continuity of **a** and **b** directions in both micas across the interfaces is inferred from the absence of sharp boundaries between the two phases.

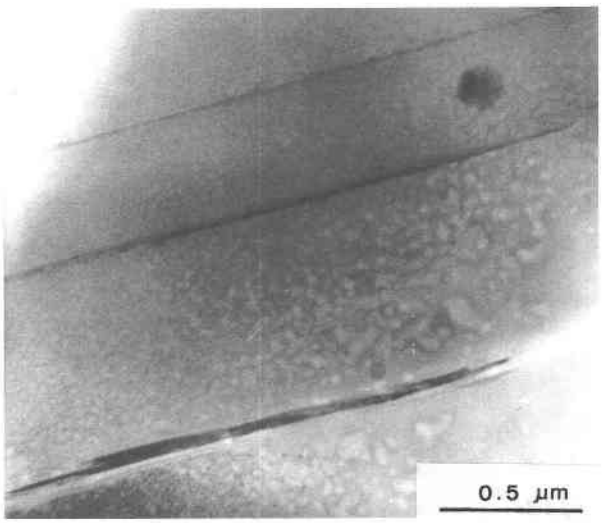

Fig. 9. Low magnification TEM image of intergrown biotite lamellae of various sizes. The thicker one (bottom) bears irregular boundaries and is surrounded by quartz rims.

come too large and would lead to the development of defects and increasingly incoherent interfaces. This allows a reduction of the strain energy but increases the surface energy (Putnis and McConnell, 1980) and is illustrated by the bending of the layers close to the interfaces of relatively small lamellae (Fig. 6). Figure 6A shows a threefold structure consisting of an inner low contrast band (quartz?) surrounded by two biotite lamellae (each about 200 Å thick) included in muscovite. Abundant edge dislocations involving (001) planes in muscovite (Fig. 6B) indicate the lack of perfectly coherent boundaries, although the dislocations might in fact be an artifact of the bending of the layers causing apparent shifting of the fringes (Guthrie and Veblen, 1989, 1990). As noted previously, the orientations of the **a** and **b** directions of adjacent muscovite-biotite pairs in this figure also appear to be the same across the two interfaces. The symmetry of this structure suggests that nucleation took place in a planar structure (stacking fault?) away from which the growth of biotite had taken place and where quartz is now located. Since the biotite layers bear only minor deformation compared with the host muscovite, their nucleation on defective areas of this type and the accommodation of both phases appear to have benefited from the already deformed structure of muscovite. The development of semicoherent to incoherent interfaces is hence inferred to have resulted from both nucleation and growth on defective areas and the early stages of the coarsening of previously semicoherent biotite intergrowths.

Coarsening. The coincidence of the **c*** axes is lost, and low angle grain boundaries develop, when biotite lamellae get thicker (more than about 500 Å). The advance of replacement across the (001) planes of the muscovite would imply that the diffusion of decomposing products proceeded approximately perpendicular to mica layers, as is indicated by diffusion halos around the intergrown phases (Fig. 5). Regardless of being an unfavorable diffusion pathway (e.g., Fortier and Giletti, 1991), this process could have been favored because of the minimization of the interfacial energy, at least while the migrating phase boundaries maintained crystallographic semicoherency. The development of incoherent boundaries and wide depletion halos in the host muscovite must have led to a change from the initial surface-controlled semicoherent growth to a growth controlled by volume diffusion. The presence of thick biotite lamellae rimmed by quartz (Fig. 9) suggests mass transfer by diffusion of dissolved species in solution through the grain interfaces and growth by precipitation from a fluid.

The above observations indicate that the progress of the decomposition reaction at a particular site was controlled by the rate of volume diffusion, although a complex picture of the reaction pathway is envisaged from the large number of intergrowths (i.e., nucleation sites), their wide range of sizes and degree of coherency (i.e., stages of growth), and the role of the continuous heterogeneous deformation and recrystallization accompanying muscovite decomposition. In any case, the close spatial relationship between the intergrowths and the diffusion halos in muscovite, the fine-grained nature of the intergrowths, and their heterogeneous distribution within the core of the primary muscovite crystals (Fig. 5) suggest that garnet decomposition was not directly related to the growth of the intergrown phases.

Pegmatitic muscovite breakdown

The reaction textures associated with the pegmatitic grains are also distinctive (Fig. 10). Fibrolitic sillimanite is associated with potassium feldspar in thin reaction rims around the muscovite crystals (Fig. 10B), whereas coarse

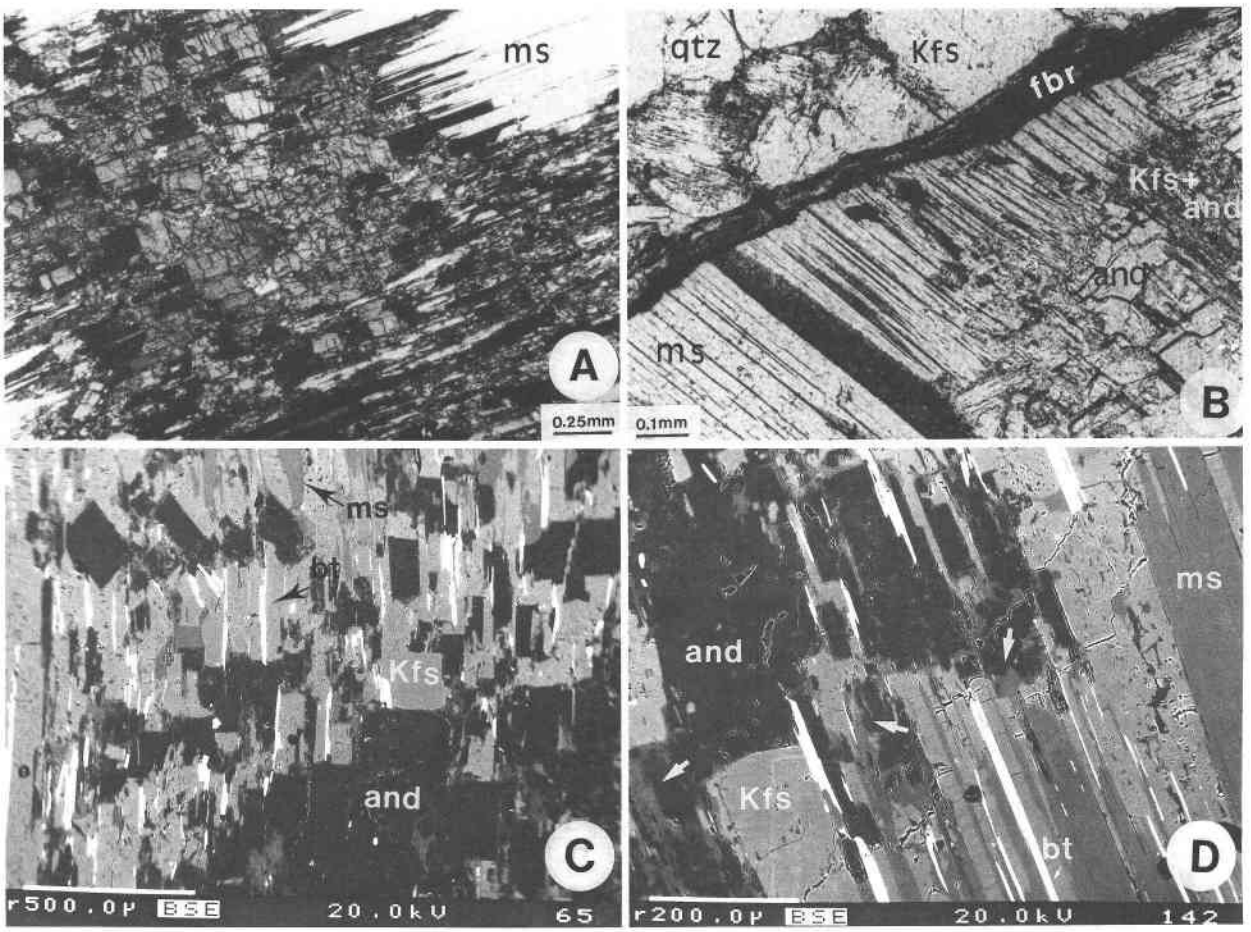

Fig. 10. Optical and BSE images of muscovite breakdown textures within a pegmatitic crystal from sample T506. (**A**) Optical image of the chessboard intergrowths of potassium feldspar (black and dark gray) and andalusite (gray and light gray) located in the core of the pegmatitic muscovite crystal (white). Partial optical continuity is indicated by simultaneous extinction of different potassium feldspar grains (crossed polarizers). (**B**) Optical image of fibrous sillimanite (fbr) and potassium feldspar around the periphery of a pegmatitic muscovite crystal in contact with quartz; a wider spot of intergrown andalusite and potassium feldspar (lower right corner) is unrelated to the fibrous sillimanite + potassium feldspar envelope (plane-polarized light). (**C**) and (**D**) BSE images of the potassium feldspar + andalusite chessboard spot shown in **A**. Skeletal andalusite (black) appears as blocky areas intergrown with potassium feldspar (light gray) and biotite (white) in the central area of the spot (**C**). Toward the rims (**D**), biotite and potassium feldspar lamellae are oriented parallel to the (001) planes of the host muscovite, causing the ragged appearance of the contact between the reactant muscovite and the product assemblage. Note the presence within the product assemblage of irregular patches of unreacted muscovite (darker gray) associated with andalusite (thicker white arrows).

andalusite and chessboard intergrowths of And + Kfs develop towards the cores of the crystals (Fig. 10B, 10C). The chessboard intergrowths are rimmed by potassium feldspar and scarce biotite growing parallel to the (001) planes of the host muscovite (Fig. 10C, 10D). The product assemblages and textural analysis indicate that this muscovite reacted through the breakdown Reaction 2b, proceeding initially at the grain contacts between muscovite and quartz to produce small amounts of Kfs + fibrous sillimanite, which partly isolated the cores of muscovite crystals from the matrix. The fact that the most extensive breakdown took place inside the muscovite crystals, away from the surrounding quartz, implies a fluid-rich environment to facilitate the transport of Si within the pegmatitic crystals; otherwise, these cores of muscovite (considered as a SiO_2-subsaturated subsystem) should not have reacted to produce andalusite.

Pegmatitic muscovite lacks indications of decomposition processes analogous to those already described for primary muscovite (i.e., through Reaction 1), probably due to its limited compositional deviations from pure muscovite. BSE inspection and qualitative traverses showed no compositional heterogeneities in the muscovite that borders the product phases, indicating that significant continuous net exchanges were not involved and hence supporting the discontinuous nature of Reaction

2b (cf. A.B. Thompson, 1982). What is notable is that (1) these muscovite samples did not react to completion, and (2) the matrix muscovite crystals lack any textural evidence for breakdown through Reaction 2b. These facts constrain the interpretation of these reaction textures in terms of the amount of overstepping required for the formation of critically sized nuclei (see below).

P-T-t EVOLUTION

Garnet-biotite (GARB) thermometry (Thompson, 1976; Ferry and Spear, 1978; Hodges and Spear, 1982; Perchuk and Larent'eva, 1983; Ganguly and Saxena, 1984; Indares and Martignole, 1985; Berman, 1990) and garnet-plagioclase-biotite-muscovite (GPBM) barometry (Ghent and Stout, 1981; Hodges and Crowley, 1985; Hoisch, 1990) were selected for *P-T* estimations in the analyzed banded gneiss (Fig. 11). Difficulties in the application of both equilibria to these rocks arise from the compositional heterogeneities displayed by the intervening phases, such that conditions of equilibrium cannot be demonstrated. The compositions used, considered to approach early equilibration conditions, are the homogeneous high-Ca garnet core, high-Ti matrix biotite, high-Si primary muscovite, and matrix plagioclase (Table 1).

A large range of temperatures (600–750 °C) are obtained when different calibrations of the GARB Fe-Mg exchange equilibrium and activity expressions are applied to the analyzed samples. Figure 11 presents the end-member *T* estimates, together with error bands (2σ) based on analytical error propagation. As a general result, the highest temperatures are obtained when garnet activity models (Hodges and Spear, 1982; Ganguly and Saxena, 1984; Berman, 1990) are included to correct the experimental calibration of Ferry and Spear (1978). Compositional corrections to account for deviations of biotite from the pure Mg-Fe system (Indares and Martignole, 1985) result in lower temperature estimates (in the range of 600–650 °C), whose error bands overlap with solutions of both the experimental calibrations (Ferry and Spear, 1978; Perchuk and Larent'eva, 1983), and the empirical calibrations (Thompson, 1976). These latter estimates are considered to approach more closely the early equilibration conditions. The empirical calibrations of the GPBM equilibrium of Hodges and Crowley (1985) and Hoisch (1990, his Reaction R6) yield pressure estimates in the range of 12–14 and 13.5–17 kbar, respectively (calculated at 650 °C; the molar volume of grossular calculated following Newton and Haselton, 1981). These estimates are considered to have low accuracy because the compositions used by these authors in their regression calculations differ significantly from those present in the analyzed banded gneisses, particularly in the case of the micas (note that Hodges and Crowley, 1985; and Hoisch, 1990, used pelitic assemblages bearing any of the Al_2SiO_5 polymorphs, so that the micas are saturated in Al). In addition, a large uncertainty arises from the possible inaccuracies of other equilibria used for the regression calibrations (Hodges and Crowley, 1985, suggested a maximum precision of ±2 kbar and ±100 °C for a given calculation). Because of these problems of precision and accuracy, no proper error propagation calculations were attempted, and Figure 11 presents the results using the calibration of Hodges and Crowley (1985). These esti-

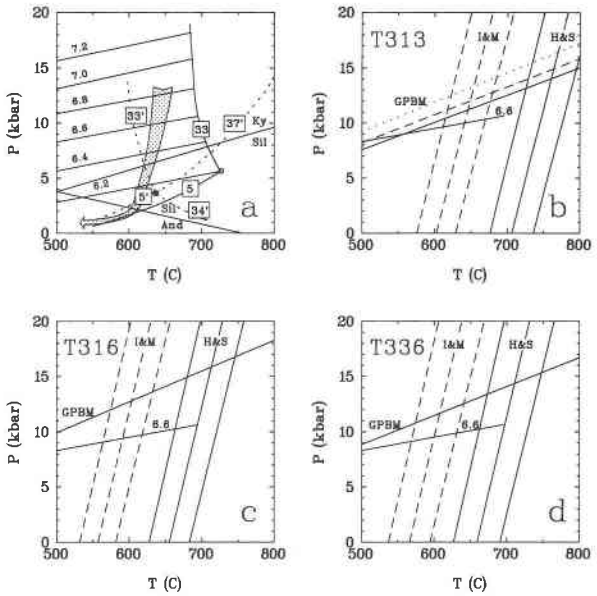

Fig. 11. (**a**) *P-T* diagram showing selected mineral and melting reactions within the KNaFMASH (dashed curves) and KFMASH (solid curves) systems. All reactions after A.B. Thompson (1982), except the Si isopleths for Reaction 1 in the text (numbers without boxes) that are after Massonne and Schreyer (1987) and the aluminum silicate transitions (after Holdaway, 1971). The remaining reactions are labeled following the numbers of A.B. Thompson (1982, his Fig. 7, written with the low-*T* assemblage to the left) as follows: 33′: Fe-Ms + Ab + Fe-Bt + Ksp + Qtz + V = L, 5′: Fe-Ms + Ab + Qtz = Kfs + Als + Fe-Bt + V, 34′: Kfs + Ab + Qtz + Fe-Bt + V = L, 37′: Fe-Ms + Ab + Qtz = Fe-Bt + Kfs + Als + L, where Als = Al_2SiO_5, V = H_2O, and L = liquid; Reactions 33 and 5 (KFMASH system) are similar to 33′ and 5′ (KNaFMASH system), respectively, but excluding Ab. Reaction 5 in this figure is Reaction 2b in the text. The dotted arrow indicates the path followed by the studied rocks, inferred from thermobarometric estimates (below), the compositional range of muscovite, and the breakdown product of pegmatitic grains. (**b**) (**c**), and (**d**) *P-T* plots of equilibria for three of the samples studied. The three curves shown for each biotite + garnet equilibrium (dashed curves labeled I&M = Indares and Martignole (1985), model A; solid curves labeled H&S = Hodges and Spear (1982) correspond to the calculated curve for the selected compositions (central line) and to 2σ error bands, based on analytical error propagation on K_d[=$(Mg/Fe)^{Grt}/(Mg/Fe)^{Bt}$]. The curves shown for garnet + plagioclase + biotite + muscovite equilibria (labeled GPBM, Hodges and Crowley, 1985) represent the selected compositions with line types, according to plagioclase type as follows: solid curve = matrix; dashed and dotted curves (sample T313) = rim and core, respectively, of plagioclase inclusion within potassium feldspar phenocryst. In all plots, the Si isopleth of Reaction 1 corresponding to Si = 6.6 atoms pfu is shown for reference.

mates do nonetheless indicate pressures greater than 10 kbar, in agreement with the Si content of matrix muscovite. The graphical celadonite barometer of Massonne and Schreyer (1987, as represented in our Fig. 11a) yields ca. 11 kbar (at 650 °C) with the maximum Si content of the analyzed primary muscovite (6.66 atoms pfu).

After these high-pressure initial conditions, decompression and lower T conditions are indicated by the lower Ca and higher Mn contents of garnet rims, either if these are considered as a growth characteristic (cf. Green, 1977) or a diffusion-induced feature at relatively high T, and by the Pl-Bt-Ms pseudomorphs after garnet, which crosscut this zonation. The compositional heterogeneities and reaction textures of muscovite also indicate that relatively large changes in P affected these rocks since the early crystallization and equilibration of primary muscovite. The decrease in Si content (6.66–6.14 atoms pfu) accompanying the decomposition and recrystallization of matrix muscovite would indicate a change in pressure from ca. 11 to 2–3 kbar (Massonne and Schreyer, 1987), whereas the breakdown of pegmatitic muscovite to And + Kfs + Bt pseudomorphs through Reaction 2b indicates that the rocks reached low pressures at relatively high temperatures, i.e., ca. 600 °C and 2 kbar (Chatterjee and Johannes, 1974; A.B. Thompson, 1982) (Fig. 11).

Although large errors may be associated with the calculated pressures and temperatures, we infer roughly 10 kbar of decompression with minor cooling (50–100 °C) (Fig. 11a). The presence of both deformed and crosscutting aplite bodies indicates that continuous ductile deformation was affecting the Torrox gneiss complex while partially molten, i.e., that the main deformational event started at high P-T and proceeded to subsolidus conditions. The processes of decomposition and recrystallization affecting the primary muscovite also suggest that deformation was taking place during decompression, as recorded by the nucleation of biotite in deformation defects. This close relationship between deformation and near isothermal decompression implies that the main deformation recorded in the TGC is associated with crustal extension rather than thickening (e.g., Thompson and Ridley, 1987), opposite to the interpretation of Cuevas et al. (1989), who associate it with nappe emplacement. Indeed, the occurrence of rapid synmetamorphic extensional tectonics associated with the main deformation event is consistent with the clustering of cooling ages of several isotopic chronometers (Rb/Sr and $^{40}Ar/^{39}Ar$ in micas and feldspars) around 21 ± 2 Ma in rocks from the TGC and adjacent metapelites (Zeck et al., 1989, 1992; Monié et al., 1991a). As an example, specimen T337, a porphyritic muscovite biotite gneiss not presented in this paper that also contains Si-rich primary and low-Si recrystallized muscovite, yields cooling ages of 22.4 ± 0.7 Ma (Rb/Sr muscovite–whole rock), 19.0 ± 0.7 Ma ($^{40}Ar/^{39}Ar$ muscovite), 20.3 ± 0.3 ($^{40}Ar/^{39}Ar$ biotite), and 20.0 ± 0.6 (low-T $^{40}Ar/^{39}Ar$ potassium feldspar), and the matrix muscovite from sample T316 yields a $^{40}Ar/^{39}Ar$ age of 19.4 ± 0.4 (Zeck et al., 1989, 1992; Monié et al., 1991a, and unpublished data). Continued rapid decompression is suggested by the depositional age of 19 ± 1 Ma for the nappe-sealing sediments of the La Viñuela formation (González-Donoso et al., 1982), which includes boulders of medium-grade graphite schists belonging to the Torrox unit (see Fig. 1). These data indicate very high rates of cooling (100–300 °C/m.y.) and uplift (2.5 to >5 km/m.y.) for the late low-P stage of the decompression path (Zeck et al., 1989, 1992; Monié et al., 1991a).

Discussion: model decomposition and breakdown reactions

Phengitic decomposition

Qualitative reaction pathway. One significant feature of the biotite-quartz intergrowths within primary muscovite is the lack of a distinct minimum size (i.e., 10^{-6}–10^{-2} mm along **c*** for the case of biotite), indicating that nucleation did not end as the reaction progressed (see Ridley, 1985). The fact that new nucleii were continuously generated during decomposition of primary muscovite is explained by (1) the continuous nature of the decomposition reaction, (2) a high decompression rate at intermediate to high pressure, and (3) a change from surface- to diffusion-controlled growth of the thicker intergrowth with the progress of reaction. Textural analysis of the reactant primary muscovite and product biotite and quartz indicates that the development of depletion halos within muscovite close to the biotite-quartz intergrowths hampered further growth and even caused the cessation of decomposition at a particular growing site when the halos had reached a critical width (in the range of 5–10 μm). The large free energy changes of reactions involving the relict high-Si compositions are proportional to the degree of overstepped conditions (Ridley and Thompson, 1986) and should have preserved and even increased the nucleation rate. This favored the progress of reaction in these not-yet-decomposed areas by further nucleation (either on continuously generated deformation defects or at random) and semicoherent growth of biotite. At the high temperature of decomposition, this reaction pathway necessitates a high decompression rate; otherwise further growth of previously formed intergrowths would have been favored rather than an extremely high number of intergrowths. This resulted in the heterogeneous spatial distribution and sizes of the product phase and of the diffusion-induced zoning in the reactant muscovite.

Under these circumstances, decomposition must have proceeded irreversibly as the relict composition of muscovite in these not-yet-decomposed areas was increasingly displaced from equilibrium during decompression (cf. Ridley and Thompson, 1986, their Fig. 4). The lack of quantitative compositional data on the finer biotite intergrowths precludes the evaluation of a hypothetical crystallization of biotite with a disequilibrium composition; however, the absence of conspicuous potassium feldspar within the intergrown assemblage could be considered an indication of a metastable decomposition pro-

TABLE 3. Components and net-transfer reactions (KTMTiASH system) describing the decomposition of primary muscovite

Phase components	Additive components	Exchange components
Muscovite (Ms)	$K_2Al_6Si_6O_{20}(OH)_4$ (Ms)	Tk, Prl, di-tri, Ti-Spl
Biotite (Bt)	$K_2Mg_6Al_2Si_6O_{20}(OH)_4$ (Phl)	Tk, Prl, di-tri, Ti □
Potassium feldspar (Kfs)	$KAlSi_3O_8$ (Or)	
Quartz (Qtz)	SiO_2 (Qtz)	
Rutile (Rt)	TiO_2 (Rt)	
Fluid	H_2O	

Net-transfer reactions (mole units)

3 Ms + 6 Tk = 4 Or + 6 Qtz + Phl + $4H_2O$	(1)
6 Or + 6 Prl = 24 Qtz	(3)
3 Ms + 6 di-tri = 3 Phl	(4)
3 Ms + 6 Ti-Spl = 3 Phl + 6 Ti □	(5)
3 Ms + 6 Ti-Spl = Phl + 6 Rt + 4 Or + $4H_2O$	(6)

Note: Exchange component abbreviations (reference is made to selected experimental investigations): Tk = $^{[4]}Si^{[6]}Mg^{[4]}Al_{-1}{}^{[6]}Al_{-1}$ (Tschermak's substitution; Velde, 1965, 1967; Monier and Robert, 1986a; Massonne and Schreyer, 1987), Ti-Spl = $^{[6]}Mg^{[6]}Ti^{[6]}Al_{-2}$ (named titanium spinel as in Dymek, 1983), Prl = $^{[4]}Si^{[12]}\square^{[12]}K_{-1}{}^{[4]}Al_{-1}$ (pyrophyllite; Velde, 1969; Rosenberg, 1987); di-tri = $^{[6]}Mg_{-3}{}^{[6]}Al_{-2}{}^{[6]}\square_{+3}$ (di-trioctahedral; Monier and Robert, 1986a; Massonne and Schreyer, 1987), Ti □ = $Ti^{[6]}\square Mg_{-2}$ (Ti □; Forbes and Flower, 1974; Abrecht and Hewitt, 1988).

cess, since Reaction 1 predicts detectable amounts of this phase. Nonetheless, as will be shown below, we interpret this major divergence among the expected and observed phase assemblage produced by the decomposition of primary muscovite in terms of (1) the effect of other components of muscovite in the final product assemblage, and (2) diffusion of K to the matrix.

Mass balance calculations and net-transfer reactions. The bulk decomposition reaction can be evaluated following the algebraic approach of J.B. Thompson (1982a, 1982b), in terms of a set of independent net-transfer reactions among independently variable components defined as linearly independent exchange vectors and additive components (Table 3). For the solid solutions of muscovite and biotite, with muscovite and phlogopite, respectively, as the additive components, the number of independent exchange vectors to be defined is six, since the number of stoichiometric and charge-balance constraints that must be satisfied is four (i.e., total positive charge = total negative charge = 44, Si + $^{[4]}$Al = 8, $^{[6]}$Al + Ti + Fe^{2+} + Mg + $^{[6]}\square$ = 6, and K + Na + $^{[12]}\square$ = 2), and the number of compositional variables in the phases is ten (cf. Labotka, 1983; Hewitt and Abrecht, 1986). For muscovite, in addition to the exchange vectors **fm** ($FeMg_{-1}$) and **nk** (NaK_{-1}), the exchange components shown in Table 3 were selected to account for the observed correlations among the components (Fig. 4, Table 2), and following the suggestions by Hewitt and Abrecht (1986). For biotite, the same exchange components were selected, except for the titanium spinel exchange, which has been substituted for the Ti-vacancy exchange (Table 3) because the amount of Ti clearly controls the amount of octahedral vacancies (see Appendix Table 2).

Since exchange reactions do not substantially modify the modal abundances of the phases involved in the reactions (J.B. Thompson, 1982b), those involving the exchange components **fm** and **nk** can be excluded from consideration by condensation of the KNaFMTiASH system into the KMTiASH system (i.e., projecting from $FeMg_{-1}$ and NaK_{-1}). This procedure is warranted by the fact that the doublets Fe-Mg and Na-K behaved similarly upon decomposition of primary muscovite (Figs. 4, 12). The

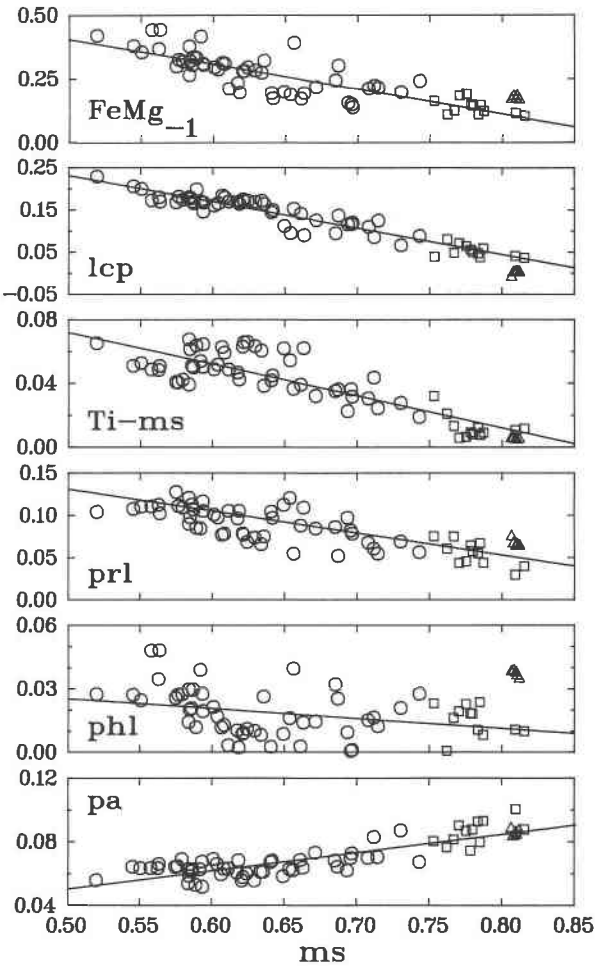

Fig. 12. Bivariate plots illustrating the compositional variations within the investigated muscovite populations (symbols as in Figs. 3, 4). The regression lines do not include the pegmatitic crystals. The seven-component cation basis (KNaFMTiAS) has been transformed into the molecular basis resulting from the operation of the exchange components mentioned in the text and Table 3 on the muscovite additive component (see Greenwood, 1975; J.B. Thompson, 1982a, for details on the procedure). In addition to muscovite, the ensuing molecular species are leucophyllite [lcp, $K_2Mg_2Al_2Si_8O_{20}(OH)_4$], titanium muscovite [Ti-ms, $K_2Mg_2Ti_2Al_2Si_6O_{20}(OH)_4$], pyrophyllite [prl, $Al_4Si_8O_{20}(OH)_4$], phlogopite (phl, $K_2Mg_6Al_2Si_6O_{20}(OH)_4$], and paragonite (pa, $Na_2Al_6Si_6O_{20}(OH)_4$]. Negative values of the leucophyllite component are obtained in the case of the pegmatitic grains, where the estimated trioctahedral and Ti components account for more Mg + Fe than its actual value. In this case, higher Fe^{3+}/Fe^{2+} ratios may have led to an overestimation of the octahedral occupancy when total Fe is expressed as Fe^{2+}.

five independent net-transfer reactions (Reactions 1, 3, 4, 5, 6, Table 3) relating the 11 selected components within the KMTiASH system can be used to describe the changes in muscovite composition and modal proportions of the product phases, but only to the extent that the selected exchange components describe compositional changes not biased by the normalization procedure. It must be noted that, in practice, the selection of a definite set of independent components is not a simple task for complex solid solutions because their number and nature depend on (1) the degree of completeness of the analyses (e.g., the availability of independent determinations of Fe^{3+}, H, and O), (2) the type of normalization used in the structural formulae (e.g., 22 O atoms vs. 8 tetrahedral plus 4 octahedral cations in muscovite), and (3) particular crystal-chemical choices (e.g., $^{[6]}$Ti vs. $^{[4]}$Ti). Additionally, once a given composition has been normalized, considerable freedom exists in the selection given the large number of potential exchange vectors (Hewitt and Abrecht, 1986). These limitations make the selected set of components nonunique, and some of the exchanges might be nonexistent (see below), but it is considered useful to model the compositional changes in muscovite during phengitic decomposition.

Mass balance calculations were done by transforming the high-Si primary muscovite cation composition (Prm, Spot 1 in Table 1) into the coordinate system defined by recrystallized muscovite (Rcrt, Spot 79 in Table 1), intergrown biotite (mean in Table 1), and stoichiometric quartz, potassium feldspar, rutile, and H_2O. The compositions were recast into the condensed KMTiASH system and expressed in terms of oxy-equivalent units (24 O units) to approximate modal abundances (cf. Brady and Stout, 1980; Thompson, 1982a). The resulting equation

$$\begin{aligned} \text{Ms (Prm)} = {} & 0.647\ \text{Ms (Rcrt)} + 0.158\ \text{Bt} \\ & + 0.089\ \text{Qtz} + 0.086\ \text{Kfs} \\ & + 0.005\ \text{Rt} + 0.016\ \text{H}_2\text{O} \end{aligned} \quad (7)$$

predicts detectable amounts of product potassium feldspar (i.e., the major solid product assemblage would be formed by 47% Bt, 27% Qtz, and 26% Kfs). As the proportions of phases expected from Reaction 1, in oxy-equivalent units, are 35% Bt, 18% Qtz, and 47% Kfs, the net effect of other components of muscovite upon decomposition has been a decrease of Kfs and an increase in Bt and Qtz, whether or not subsequent diffusion modified the predicted values. Recasting the compositions in Reaction 7 in terms of the components shown in Table 3 yields (in mole units)

$$\begin{aligned} & 3\ \text{Ms} + 4.510\ \text{Tk} + 1.130\ \text{Prl} \\ & + 0.500\ \text{di-tri} + 0.990\ \text{Ti Spl} \\ & = 1.342\ \text{Phl} + 0.527\ \text{Ti}\square + 2.185\ \text{Or} \\ & \quad + 9.031\ \text{Qtz} + 0.463\ \text{Rt} + 3.315\ \text{H}_2\text{O}. \end{aligned} \quad (8)$$

Reaction 8 can be considered as a weighted bulk decomposition reaction made up of the simpler net-transfer Reactions 1, 3, 4, 5, and 6 corrected by ⅙ of the corresponding stoichiometric coefficients of the exchange vectors on the left side of Equation 8 (note that the Ti-Spl exchange has not been split into its corresponding values involved in Equations 5 and 6, but the correction factors for these equations equal ⅙ of the stoichiometric coefficients of the Ti-□ and Rt components, respectively). The normalized values of these coefficients in Equation 8 are 63.3% Tk, 15.8% Prl, 7.0% di-tri, and 13.9% Ti-Spl, indicating that the phengitic muscovite decomposition in Reaction 1 accounts for most of the product phases and changes in composition of the matrix muscovite. However, the changes in Ti and the trioctahedral components in muscovite through Reactions 5 and 4, respectively, contributed mostly in the production of biotite, and the change in the alkali content of muscovite, monitored by the pyrophyllite exchange through Reaction 3, contributed to the production of more quartz and less potassium feldspar. This is illustrated in the condensed AKM projection of Figure 13, where the observed compositional trend is located in the middle of the trends anticipated for each of the four exchange vectors operating in muscovite (or five net-transfer reactions). Since the composition of primary muscovite undergoing decomposition (assemblage A in Fig. 13) appears displaced towards the Al-Phl-Ms join of the Al-Phl-Ms-Kfs triangle, lower amounts of Kfs would have been produced (ca. 25% of the product solid phases vs. 47% predicted by Reaction 1, in oxy-equivalent units). This is largely the result of the increasing alkali contents in matrix muscovite as decomposition proceeds (Figs. 4, 12).

The above results are probably inaccurate because they depend on the value of the selected set of exchange vectors, which, in turn, critically depends on the value of the normalization procedure and the lack of estimates of independent Fe^{3+} and H. Particularly important in this context is the lack of H estimates and the existence of the pyrophyllite component in muscovite. As long as the interlayer cations correlated with other compositional variables in the studied muscovite samples (Table 2), care was taken to avoid alkali loss during the microprobe analyses (Fig. 2); other elements, such as Ba, Sr, or Cs, were found to be below the normal quantitation limits (i.e., in amounts less than about 0.01 wt%), and the calculated A-site deficiency (ranging from 0.256 to 0.058 atoms pfu) must be explained as vacancies (Velde, 1969; Rosenberg, 1987) or the possible occurrence of H_3O^+ or H_2O in the interlayer sites (i.e., the hydronium substitution $H_3O^+K_{-1}$; see Dyar et al., 1991, and references therein). The negative correlation of interlayer cations and Si (Fig. 4, Table 2) would favor the occurrence of actual vacancies (i.e., the pyrophyllite substitution) but only to the extent that the hydronium contents had not been sensitive to the changes in *P-T* that triggered muscovite decomposition. This cannot be ruled out, given the evidence for H and O variations in biotite with metamorphic grade and assemblage as reported by Dyar et al. (1991). It is worthwhile to note that the pegmatitic muscovite, believed to have formed close to the H_2O-saturated granite solidus,

bears low alkali contents as compared with those of the recrystallized matrix muscovite, suggesting higher H contents in the interlayer sites. In fact, if H_3O^+ or H_2O fill the interlayer vacancies, reactions of the type

$$9\ Or + 6H_3O^+K_{-1}\ [Ms] = 1.5\ Ms + 18\ Qtz + 6H_2O \quad (9)$$

can also explain both the progressive increase of alkali cations in matrix muscovite with the progress of decomposition and a decrease in the evolved potassium feldspar components relative to that expected through Reaction 1. Thus, although we have followed other workers (e.g., Wang and Banno, 1987) in modeling the A-site changes through the pyrophyllite substitution due to the lack of independent estimations of H, the calculated pyrophyllite component (Fig. 12) and the relative contribution of Equation 3 to the bulk decomposition Reaction 8 must be seen at best as a composite estimate of the effect of both the pyrophyllite and the hydronium substitutions. Nonetheless, the compositional data presented confirm that variations in the interlayer sites attended the phengitic decomposition of matrix muscovite.

The lack of potassium feldspar occurring as intergrowths within primary muscovite grains contradicts the predictions of phase equilibrium considerations and the mass balance calculations (Eqs. 7, 8). The preferred explanation is that K had diffused to the groundmass, the more so when an aqueous fluid phase evolved as decomposition proceeded. Diffusion of K through primary muscovite crystals can be rationalized as a hydrated compound dissolved in the fluid, implying that hydrolysis reactions like

$$6\ Or + 4H_2O = Ms + 12\ Qtz + 4KOH\ (fluid) \quad (10)$$

actually represented steps of the molecular reactions. In this regard, the increase in the alkali content of primary muscovite as decomposition proceeds can be envisaged to have taken place through exchange with the K-bearing fluid through the simple reaction

$$KOH\ (fluid) + H_3O^+K_{-1}\ (Ms) = 2H_2O \quad (11)$$

favoring the operation of the hydronium substitution in these micas. More precise compositional data are needed to evaluate the relative importance of the pyrophyllite and hydronium substitutions.

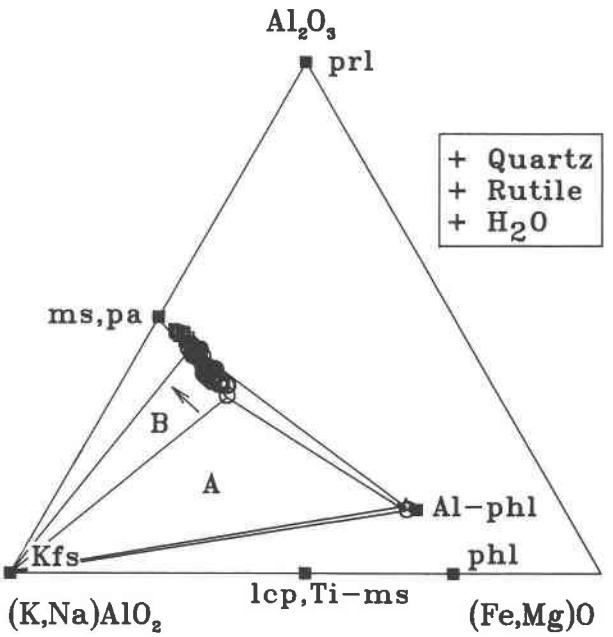

Fig. 13. Condensed AKM plot of analyses of primary (circles) and recrystallized (squares) muscovite, high-Ti (Ti > 0.3 atoms pfu; circle) matrix, and intergrown (star) biotite (Table 1), projected through SiO_2, TiO_2, and H_2O, and showing the schematic phase relations (KMASH system) relevant to primary muscovite decomposition [abbreviations as in Fig. 12, except Al-phl: aluminum phlogopite, $K_2{}^{[6]}Al_1Mg_5Al_3Si_5O_{20}(OH)_4$]. The three-phase field A, defined by potassium feldspar, muscovite bearing the maximum Si content (6.66 atoms pfu), and high titanium matrix biotite represents the early equilibration assemblage. As decomposition of primary muscovite proceeds, the three-phase field expands (arrow), as represented by the three-phase field B defined by potassium feldspar, low-Si primary muscovite and intergrown biotite. The compositional deviations of muscovite undergoing decomposition from the ms-lcp join toward pyrophyllite and phlogopite end-members would produce less potassium feldspar upon decomposition relative to the amounts predicted by Reaction 1 (note also that the deviations of muscovite due to the Tk and Ti-Spl exchanges are collinear due to the projection through TiO_2). When projected into this diagram, the compositions of the heterogenous matrix biotite overlap the aluminous biotite end-member.

Muscovite breakdown

Rubie and Brearley (1987) and Brearley and Rubie (1990, e.g., their Fig. 5) observed topotactic and skeletal textures in muscovite that suffered disequilibrium breakdown by metastable melting in laboratory experiments (see also Brearley, 1986, for a natural case of metastable breakdown). These authors obtained complete breakdown of muscovite within 2–20 weeks for H_2O-saturated and H_2O-undersaturated systems, under strongly overstepped experimental conditions (50–200 °C) at low *P* (1 kbar), and observed that the stable Kfs + Sil + Bt assemblage developed only under H_2O-undersaturated conditions. These results would indicate rapid growth for the topotactic and chessboard textures of the And + Kfs + Bt pseudomorphs developed in the pegmatitic muscovite grains (Fig. 10), although the strongly overstepped conditions for the Equilibrium 2 investigated by Rubie and Brearley (1987) and Brearley and Rubie (1990) make both cases not strictly comparable. However, Schramke et al. (1987) obtained the stable assemblage And + Kfs under moderate overstepping (0–100 °C, at 0.5–5 kbar) and H_2O-saturated conditions and concluded that Reaction 2 should quickly proceed to completion during prograde metamorphism, even at conditions very close to the equilibrium boundary, if the rate-controlling step (a surface-controlled rate involving andalusite surfaces; see

also Kerrick et al., 1991) remains unchanged through the reaction progress. Also, Ridley and Thompson (1986) estimated a wide range of temperature overstepping required for nucleation in the breakdown of muscovite (Ms + Qtz = Sil + Kfs + H_2O) as a function of interfacial energy and based on selected seeded and unseeded experimental studies at 2 kbar, but they suggested the generalized values of ca. 10 °C and 1 kbar for dehydration reactions. These experimental and theoretical evidences for low overstepping required for nucleation and high reaction rates conflict with the fact that Reaction 2 did not progress to completion in most of the observed pegmatitic muscovite crystals. But perhaps even more surprising is the fact that primary and recrystallized matrix muscovite crystals do not bear any textural evidence for breakdown through Reaction 2, in spite of the presence of incompatible fine-grained quartz intergrown within them.

The interpretation of the sequential growth of fibrous sillimanite and andalusite in terms of a change from the sillimanite to the andalusite stability fields with the reaction progress is further complicated by the metastable nature of fibrolitic sillimanite, which might have grown outside the sillimanite stability field (cf. Kerrick, 1990). However, the decompression path followed by these rocks (evolving from the kyanite, to the sillimanite, to the andalusite stability fields, see Fig. 11) is consistent with initial growth of fibrous sillimanite close to Equilibrium 2. The progress of the reaction, involving andalusite, must also have taken place close to the equilibrium boundary, otherwise muscovite would have reacted completely within the andalusite stability field, according to the experimental evidence cited above. This and the fact that the amount of overstepping of Equilibrium 2 was not adequate for the activation of nucleation in the primary and recrystallized matrix crystals indicate that cooling accompanied decompression at this stage of the *P-T* evolution and that the *P-T* path evolved close to Equilibrium 2. Additionally, kinetic factors affecting the reaction pathway (e.g., a change from surface-controlled to diffusion-controlled growth?) could help explain the lack of complete breakdown. However, to explain the contrasting behavior of matrix and pegmatitic muscovite crystals, modest displacements in the *P-T* space of Equilibrium 2 due to compositional differences of the phases, including the fluid, seem to be required. The virtually identical compositions of recrystallized and pegmatitic grains in the analyzed samples (Fig. 4) and the fact that muscovite breakdown textures have been observed only in aplitic and pegmatitic bodies within the TGC suggest that variations in the local fluid composition could be the major factor affecting the onset of breakdown. Important compositional variables of the local fluids in equilibrium with these rocks include the activity of ionic species (i.e., K^+, Na^+, H^+; e.g., Wintsch, 1975) and of B and F (Manning and Pichavant, 1983; Pichavant, 1987). The onset of the breakdown of the pegmatitic muscovite should be promoted at higher *P* by a lowered a_{H_2O} caused by the presence of B or F (note the coexistence of tourmaline) or the infiltration from the matrix of a fluid with a lowered a_{K^+}/a_{H^+} ratio (Wintsch, 1975, his Fig. 2) in the pegmatitic structure.

Concluding remarks

The instability of the leucophyllite component in matrix muscovite upon decompression is in accordance with other investigations on natural and experimental systems under subsolidus conditions. However, the high Si values found in the primary muscovite of the TGC stand as exceptional when compared with typical compositions of high-grade muscovite (e.g., Si = 6.2–6.3; Miller et al., 1981). Further, both the estimated *P-T* conditions of early equilibration (600–650 °C, >10 kbar) and the presence of concordant and crosscutting aplites strongly suggest that primary muscovite within the banded gneisses had been in equilibrium with a melt during this stage. Examples of anatectic granites either emplaced or generated at high pressure and bearing high-Si muscovite are not common. However, the intrusive anatectic leucogranites emplaced in kyanite-bearing peraluminous granitic gneisses in the Higher Himalayas (Searle and Fryer, 1986) also bear muscovite with high Si contents (6.48 atoms pfu), which is consistent with our observations and interpretation of the TGC as an instance of high-pressure melting within a markedly thickened crust.

The data presented in this paper indicate that the compositional behavior of high-*T* muscovite is *P*-sensitive, resembling that of lower grade environments, although very high *P* conditions and high decompression rates would possibly be required to detect this effect in natural instances because of the increased probability that complete reequilibration takes place at low pressure during high-*T* emplacement or exhumation of granites and anatectites. In the *P-T-t* path, section radiometric evidence was summarized, indicating that high decompression rates characterized the low-*P* portion (<2–3 kbar) of the *P-T* path depicted in Figure 11. Although more difficult to evaluate quantitatively, the reaction textures, and specifically the evidence for continuous nucleation and the preservation of relict Si-rich compositions in primary muscovite from the TGC, may be taken as a strong indication that high decompression rates were also prevalent during the earlier stage. This makes conceivable that the age of the pressure peak in the Alpujarride series would not have been far in time from the low-*P* cooling ages clustering at 21 ± 2 Ma. In this regard it is worth mentioning that a $^{40}Ar/^{39}Ar$ age of 25.4 ± 0.4 Ma was reported by Monié et al. (1991b), after a low-*T* phengite coexisting with carpholite, aragonite, and chloritoid in a sample from the Alpujarride Trevenque unit (located 50 km to the northeast of the TGC), which was meant to mark the "end of the underthrusting processes in the Alpujarride nappes and the beginning of exhumation." If that were the case, an average uplift rate of about 10 km/m.y. is easily derived for the whole decompression trajectory of Figure 11, which illustrates what kind of ex-

treme geological conditions accompanied the production of the muscovite textures reported in this study.

Acknowledgments

We wish to thank C.V. Guidotti, D.R. Veblen, and H.J. Massonne for their suggestions and comments on an earlier version of the manuscript, and J.T. Cheney, G. Guthrie, and Associate Editor J.B. Brady for their constructive reviews, which contributed substantially to the article's improvement. Thanks are also given to D.S. Silverberg for his comments and help with the English version and M.A. Hidalgo Laguna for his careful attention to the microprobe analyses. The results presented in this paper form part of a Ph.D. thesis by A.G.C. This study has received financial support from the Spanish CAICYT (project PB89-0017, A.G.C. and R.L.T.R., and project PB87-022801, A.S.N.) and from the Junta de Andalucia (research groups 4065, A.S.N., and 4072, A.G.C. and R.L.T.R.).

References cited

Abrecht, J., and Hewitt, D.A. (1988) Experimental evidence on the substitution of Ti in biotite. American Mineralogist, 73, 1275–1284.

Berman, R.G. (1990) Mixing properties of Ca-Mg-Fe-Mn garnets. American Mineralogist, 75, 328–344.

Brady, J.B., and Stout, J.H. (1980) Normalization of thermodynamic properties and some implications for graphical and analytical problems in petrology. American Journal of Science, 280, 173–189.

Brearley, A.J. (1986) An electron optical study of muscovite breakdown in pelitic xenoliths during pyrometamorphism. Mineralogical Magazine, 50, 385–397.

Brearley, A.J., and Rubie, D.C. (1990) Effects of H_2O on the disequilibrium breakdown of muscovite + quartz. Journal of Petrology, 31, 925–956.

Chatterjee, N.D., and Froese, E. (1975) A thermodynamic study of the pseudobinary join muscovite-paragonite in the system $KAlSi_3O_8$-$NaAlSi_3O_8$-Al_2O_3-SiO_2-H_2O. American Mineralogist, 60, 985–993.

Chatterjee, N.D., and Johannes, W. (1974) Thermal stability and standard thermodynamic properties of synthetic $2M_1$-muscovite, $KAl_2[AlSi_3O_{10}(OH)_2]$. Contributions to Mineralogy and Petrology, 48, 89–114.

Cipriani, C., Sassi, F.P., and Scolari, A. (1971) Metamorphic white micas: Definition of paragenetic fields. Schweizerische mineralogische und petrographische Mitteilungen, 51, 259–302.

Cuevas, J., Navarro-Vilá, F., and Tubía, J.M. (1989) Interprétation des cisaillements ductiles vers le NE dans les gneiss de Torrox (Complexe Alpujarride, Cordillères Bétiques). Geodinamica Acta, 3, 107–116.

Dyar, M.D., Colucci, M.T., and Guidotti, C.V. (1991) Forgotton major elements: Hydrogen and oxygen variation in biotite from metapelites. Geology, 19, 1029–1032.

Dymek, R.F. (1983) Titanium, aluminum and interlayer cation substitutions in biotite from high-grade gneisses, West Greenland. American Mineralogist, 68, 880–899.

Eggleton, R.A., and Buseck, P.R. (1980) High resolution electron microscopy of feldspar weathering. Clays and Clay Minerals, 28, 173–178.

Elorza, J.J., and García-Dueñas, V. (1981) Hoja y memoria explicativa de Vélez-Málaga. Mapa Geológico de España, escala 1:50000. Instituto Geológico y Minero de España, Madrid.

Ernst, W.G. (1963) Significance of phengitic micas from low grade schists. American Mineralogist, 48, 1357–1373.

Evans, B.W., and Guidotti, C.V. (1966) The sillimanite-potash feldspar isograd in western Maine, USA. Contributions to Mineralogy and Petrology, 12, 25–62.

Evans, B.W., and Patrick, B.E. (1987) Phengite-$3T$ in high-pressure metamorphosed granitic orthogneisses, Seward Peninsula, Alaska. Canadian Mineralogist, 25, 141–158.

Ferrow, E.A., London, D., Goodman, K.S., and Veblen, D.R. (1990) Sheet silicates of the Lawler Peak granite, Arizona: Chemistry, structural variations, and exsolution. Contributions to Mineralogy and Petrology, 105, 491–501.

Ferry, J.M., and Spear, F.S. (1978) Experimental calibration of the partitioning of Fe and Mg between biotite and garnet. Contributions to Mineralogy and Petrology, 66, 113–117.

Fletcher, C.J.N., and Greenwood, H.J. (1979) Metamorphism and structure of the Penfold Creek Area, near Quesnel Lake, British Columbia. Journal of Petrology, 20, 743–794.

Forbes, W.C., and Flower, M.F.J. (1974) Phase relations of titan-phlogopite, $K_2Mg_4TiAl_2Si_7O_{20}(OH)_4$: A refractory phase in the upper mantle? Earth and Planetary Science Letters, 22, 60–66.

Fortier, S.M., and Giletti, B.J. (1991) Volume self-diffusion of oxygen in biotite, muscovite, and phlogopite micas. Geochimica et Cosmochimica Acta, 55, 1319–1330.

Franz, G., Thomas, S., and Smith, D.C. (1986) High-pressure phengite decomposition in the Weissenstein eclogite, Münchberger Gneiss Massif, Germany. Contributions to Mineralogy and Petrology, 92, 71–85.

Ganguly, J., and Saxena, S.K. (1984) Mixing properties of aluminosilicate garnets: Constraints from natural and experimental data, and applications to geothermo-barometry. American Mineralogist, 69, 88–97.

Ghent, E.D., and Stout, M.Z. (1981) Geobarometry and geothermometry of plagioclase-biotite-garnet-muscovite assemblages. Contributions to Mineralogy and Petrology, 76, 92–97.

González-Donoso, J.M., Linares, D., Molina, E., Serrano, F., and Vera, J.A. (1982) Sobre la edad de la Formación de la Viñuela (Cordilleras Béticas, Provincia de Málaga). Boletín de la Real Sociedad Española de Historia Natural, 80, 255–275.

Green, T.H. (1977) Garnet in silicic liquids and its possible use as a P-T indicator. Contributions to Mineralogy and Petrology, 65, 59–67.

Greenwood, H.J. (1975) Thermodynamically valid projections of extensive phase relationships. American Mineralogist, 60, 1–8.

Guidotti, C.V. (1973) Compositional variation in muscovite as a function of metamorphic grade and assemblage in metapelites from N.W. Maine. Contributions to Mineralogy and Petrology, 42, 33–42.

——— (1978a) Compositional variation of muscovite in medium- to high-grade metapelites of northwestern Maine. American Mineralogist, 63, 878–884.

——— (1978b) Muscovite and K-feldspar from two-mica adamellite in northwestern Maine: Composition and petrogenetic implications. American Mineralogist, 63, 750–753.

——— (1984) Micas in metamorphic rocks. In Mineralogical Society of America Reviews in Mineralogy, 13, 357–468.

Guidotti, C.V., and Sassi, F.P. (1976) Muscovite as a petrogenetic indicator mineral in pelitic schists. Neues Jahrbuch für Mineralogie Abhandlungen, 127, 97–142.

Guthrie, G.D., Jr., and Veblen, D.R. (1989) High-resolution transmission electron microscopy of mixed-layer illite/smectite: Computer simulations. Clays and Clay Minerals, 37, 1–11.

——— (1990) Interpreting one-dimensional high-resolution transmission electron micrographs of sheet silicates by computer simulations. American Mineralogist, 75, 276–288.

Heinrich, C.A. (1982) Kyanite-eclogite to amphibolite facies evolution of hydrous mafic and pelitic rocks. Adula nappe, Central Alps. Contributions to Mineralogy and Petrology, 81, 30–38.

Hewitt, D.A., and Abrecht, J. (1986) Limitations on the interpretation of biotite substitutions from chemical analyses of natural samples. American Mineralogist, 71, 1126–1128.

Hodges, K.V., and Crowley, P.D. (1985) Error estimation and empirical geobarometry for pelitic systems. American Mineralogist, 70, 702–709.

Hodges, K.V., and Spear, F.S. (1982) Geothermometry, geobarometry, and the Al_2SiO_5 triple point at Mt. Moosilauke, New Hampshire. American Mineralogist, 67, 1118–1134.

Hoisch, T.D. (1990) Empirical calibration of six geobarometers for the mineral assemblage quartz + muscovite + biotite + plagioclase + garnet. Contributions to Mineralogy and Petrology, 104, 225–234.

Holdaway, M.J. (1971) Stability of andalusite and the aluminum-silicate phase diagram. American Journal of Science, 271, 97–131.

Holdaway, M.J., Dutrow, B.L., and Hinton, R.W. (1988) Devonian and Carboniferous metamorphism in west-central Maine: The muscovite-almandine geobarometer and the staurolite problem revisited. American Mineralogist, 73, 20–47.

Iijima, S., and Zhu, J. (1982) Electron microscopy of a muscovite-bioite interface. American Mineralogist, 67, 1195–1205.

Indares, A., and Martignole, J. (1985) Biotite-garnet geothermometry in granulite facies: The influence of Ti and Al in biotite. American Mineralogist, 70, 272–278.

Kerrick, D.M. (1972) Experimental determination of muscovite + quartz stability with $P_{H_2O} < P_{total}$. American Journal of Science, 272, 946–958.

——— (1990) The Al_2SiO_5 polymorphs. Mineralogical Society of America Reviews in Mineralogy, 22, 406 p.

Kerrick, D.M., Lasaga, A.C., and Raeburn, S.P. (1991) Kinetics of heterogeneous reactions. In Mineralogical Society of America Reviews in Mineralogy, 26, 583–671.

Kistler, R.W., Ghent, E.D., and O'Neil, J.R. (1981) Petrogenesis of garnet two-mica granites in the Ruby Mountains, Nevada. Journal of Geophysical Research, 86, 10591–10606.

Konings, R.J.M., Boland, J.N., Vriend, S.P., and Jansen, J.B.H. (1988) Chemistry of biotites and muscovites in the Abas granite, northern Portugal. American Mineralogist, 73, 754–765.

Kretz, R. (1983) Symbols for rock-forming minerals. American Mineralogist, 68, 277–279.

Labotka, T.C. (1983) Analysis of compositional variations of biotite in pelitic hornfelses from northeastern Minnesota. American Mineralogist, 68, 900–914.

Lasaga, A.C. (1981) The atomistic basis of kinetics: Defects in minerals. In Mineralogical Society of America Reviews in Mineralogy, 8, 261–319.

Lee, D.E., Kistler, R.W., Friedman, I., and Van Loenen, R.E. (1981) Two-mica granites of northeastern Nevada. Journal of Geophysical Research, 86, 10607–10616.

Loomis, T.P. (1976) Irreversible reactions in high-grade metapelitic rocks. Journal of Petrology, 17, 559–588.

——— (1979) A natural example of metastable reactions involving garnet and sillimanite. Journal of Petrology, 20, 271–292.

Manning, D.A.C., and Pichavant, M. (1983) The role of fluorine and boron in the generation of granitic melts. In M.P. Atherton and C.D. Gribble, Eds., Migmatites, melting and metamorphism, p. 94–109. Shiva Publishing, Nantwich, England.

Massonne, H.J., and Schreyer, W. (1986) High-pressure syntheses and X-ray properties of white micas in the system K_2O-MgO-Al_2O_3-SiO_2-H_2O. Neues Jahrbuch für Mineralogie Abhandlungen, 153, 177–215.

——— (1987) Phengite geobarometry based on the limiting assemblage with K-feldspar, phlogopite, and quartz. Contributions to Mineralogy and Petrology, 96, 212–224.

Miller, C.F., Stoddard, E.F., Bradfish, L.J., and Dollase, W.A. (1981) Composition of plutonic muscovite: Genetic implications. Canadian Mineralogist, 19, 25–34.

Miyashiro, A., and Shido, F. (1985) Tschermak substitution in low- and middle-grade pelitic schists. Journal of Petology, 26, 449–487.

Monié, P., Torres-Roldán, R.L., García-Casco, A., and Goffé, B. (1991a) High rates of cooling in the western Alpujarrides, Betic Cordilleras, southern Spain: A $^{40}Ar/^{39}Ar$ study. Terra Nova Abstract, 3 (suppl. 6), 8.

Monié, P., Galindo-Zaldívar, J., González-Lodeiro, F., Goffé, B., and Javaloy, A. (1991b) $^{40}Ar/^{39}Ar$ geochronology of Alpine tectonism in the Betic Cordilleras (southern Spain). Journal of the Geological Society of London, 148, 288–297.

Monier, G., and Robert, J.L. (1986a) Muscovite solid solutions in the system K_2O-MgO-FeO-Al_2O_3-SiO_2-H_2O: An experimental study at 2 kbar PH_2O and comparison with natural Li-free white micas. Mineralogical Magazine, 50, 257–266.

——— (1986b) Titanium in muscovites from two mica granites: Substitutional mechanisms and partition with coexisting biotites. Neues Jahrbuch für Mineralogie Abhandlungen, 153, 147–161.

Monier, G., Mergoil-Daniel, J., and Labernardière, H. (1984) Générations succesives de muscovites et feldspaths potassiques dans les leucogranites du massif de Millevaches (Massif Central français). Bulletin de Minéralogie, 107, 55–68.

Newton, R.C., and Haselton, H.T. (1981) Thermodynamics of the garnet-plagioclase-Al_2SiO_5-quartz geobarometer. Advances in Physical Geochemistry, 1, 129–145.

Perchuk, L.L., and Larent'eva, I.V. (1983) Experimental investigation of exchange equilibria in the system cordierite-garnet-biotite. Advances in Physical Geochemistry, 3, 199–239.

Pichavant, M. (1987) Effects of B and H_2O on liquidus phase relations in the haplogranite system at 1 kbar. American Mineralogist, 72, 1056–1070.

Pouchou, J.L., and Pichoir, F. (1985) "PAP" $\phi(\rho z)$ procedure for improved quantitative microanalysis. In J.T. Armstrong, Ed., Microbeam Analysis, p. 104. San Francisco Press, San Francisco.

Price, R.C. (1983) Geochemistry of a peraluminous granitoid suite from north-eastern Victoria, south-eastern Australia. Geochimica et Cosmochimica Acta, 47, 31–42.

Putnis, A., and McConnell, J.D.C. (1980) Principles of mineral behavior, 257 p. Blackwell, Oxford.

Ridley, J. (1985) The effect of reaction enthalpy on the progress of a metamorphic reaction. Advances in Physical Geochemistry, 4, 80–97.

Ridley, J., and Thompson, A.B. (1986) The role of mineral kinetics in the development of metamorphic microtextures. Advances in Physical Geochemistry, 5, 154–193.

Robinson, P., Jaffe, H.W., Ross, M., and Klein, C., Jr. (1971) Orientation of exsolution lamellae in clinopyroxenes and clinoamphiboles: Consideration of optimal phase boundaries. American Mineralogist, 56, 909–939.

Rosenberg, P.H. (1987) Synthetic muscovite solid solutions in the system K_2O-Al_2O_3-SiO_2-H_2O. American Mineralogist, 72, 716–723.

Rubie, D.C., and Brearley, A.J. (1987) Metastable melting during the breakdown of muscovite + quartz at 1 kbar. Bulletin de Minéralogie, 110, 533–549.

Saliot, P., and Velde, B. (1982) Phengite compositions and post-nappe high-pressure metamorphism in the Pennine zone of the French Alps. Earth and Planetary Science Letters, 57, 133–138.

Sanz de Galdeano, C. (1989) Estructura de las Sierras de Tejeda y de Cómpeta (Conjunto Alpujárride, Cordilleras Béticas). Revista de la Sociedad Geológica de España, 2, 77–84.

Schramke, J.A., Kerrick, D.M., and Lasaga, A.C. (1987) The reaction muscovite + quartz = andalusite + K-feldspar + water. Part 1. Growth kinetics and mechanism. American Journal of Science, 287, 517–559.

Searle, M.P., and Fryer, B.J. (1986) Garnet, tourmaline and muscovite-bearing leucogranites, gneisses and migmatites of the Higher Himalayas from Zanskar, Kulu, Lahoul and Kashmir. The Geological Society Special Publication, 19, 185–201.

Sevigny, J.H., Parrish, R.R., and Ghent, E.D. (1989) Petrogenesis of peraluminous granites, Monashee Mountains, southern Canadian Cordillera. Journal of Petrology, 30, 557–581.

Speer, J.A. (1982) Metamorphism of pelitic rocks of the Snyder Group in the contact aureole of the Kigalpait layered intrusion, Labrador: Effects of buffering partial pressures of water. Canadian Journal of Earth Sciences, 19, 1888–1909.

——— (1984) Micas in igneous rocks. In Mineralogical Society of America Reviews in Mineralogy, 13, 229–356.

Thompson, A.B. (1976) Mineral reactions in pelitic rocks II. Calculation of some *P-T-X* (Fe-Mg) phase relations. American Journal of Science, 276, 425–454.

——— (1982) Dehydration melting of pelitic rocks and the generation of H_2O-undersaturated granitic liquids. American Journal of Science, 282, 1567–1595.

Thompson, A.B., and Ridley, J.R. (1987) Pressure-temperature-time (*P-T-t*) histories of orogenic belts. Philosophical Transactions of the Royal Society of London, A 321, 27–45.

Thompson, J.B., Jr (1979) The Tschermak substitution and reaction in pelitic schists. In V.A. Zharikov, V.I. Fonorev, and J.P. Korikovskii, Eds., Problems in physicochemical petrology, p. 146–159. Academy of Sciences, Moscow (in Russian).

——— (1982a) Compositional space: An algebraic and geometric approach. In Mineralogical Society of America Reviews in Mineralogy, 10, 1–31.

——— (1982b) Reaction space: An algebraic and geometric approach. In Mineralogical Society of America Reviews in Mineralogy, 10, 33–52.

Torres-Roldán, R.L. (1974) El metamorfismo progresivo y la evolución de la serie de facies en las metapelitas alpujárrides al SE de Sierra Almijara (sector central de las Cordilleras Béticas. S de España). Cuadernos de Geología, 5, 21–77.

——— (1979) The tectonic subdivision of the Betic Zone (Betic Cordillera, S. Spain): Its significance and one possible geotectonic scenario for the westernmost Alpine Belt. American Journal of Science, 279, 19–51.

——— (1981) Plurifacial metamorphic evolution of the Sierra Bermeja peridotite aureole (southern Spain). Estudios Geológicos, 37, 115–133.
Tracy, R. (1978) High grade metamorphic reactions and partial melting in pelitic schists, west-central Massachusetts. American Journal of Science, 278, 150–178.
Veblen, D.R. (1983) Microstructures and mixed layering in intergrown wonesite, chlorite, talc, biotite, and kaolinite. American Mineralogist, 68, 566–580.
Velde, B. (1965) Phengite micas: Synthesis, stability, and natural occurrence. American Journal of Science, 263, 886–913.
——— (1967) Si^{+4} content of natural phengites. Contributions to Mineralogy and Petrology, 14, 250–258.
——— (1969) The compositional join muscovite-pyrophyllite at moderate pressures and temperatures. Bullétin de la Societé Française de Minéralogie et de Cristallographie, 92, 360–368.
Wang, G.F., and Banno, S. (1987) Non-stoichiometry of interlayer catyions in micas from low- to middle-grade metamorphic rocks in the Ryoke and the Sanbagawa belts, Japan. Contributions to Mineralogy and Petrology, 97, 313–319.
Weiss, Z., Rieder, M., Chmielová, M., and Krajícek, J. (1985) Geometry of the octahedral coordination in micas: A review of refined structures. American Mineralogist, 70, 747–757.
Wintsch, R.P. (1975) Solid-fluid equilibria in the system $KAlSi_3O_8$-$NaAlSi_3O_8$-Al_2SiO_5-SiO_2-H_2O-HCl. Journal of Petrology, 16, 57–79.
Wise, W.S., and Eugster, H.P. (1964) Celadonite: Synthesis, thermal stability and occurrence. American Mineralogist, 49, 1031–1083.
Zeck, H.P., Albat, F., Hansen, B.T., Torres-Roldán, R.L., García-Casco, A., and Martín-Algarra, A. (1989) A 21 ± 2 Ma age for the termination of the ductile Alpine deformation in the internal zone of the Betic Cordilleras, south Spain. Tectonophysics, 169, 215–220.
Zeck, H.P., Monié, P., Villa, I., and Hansen, B.T. (1992) Very high rates of cooling and uplift in the Alpine belt of the Betic Cordilleras, southern Spain. Geology, 20, 79–82.
Zussman, J. (1979) The crystal chemistry of the micas. Bulletin de Minéralogie, 102, 5–13.

Manuscript received September 9, 1991
Manuscript accepted August 26, 1992